Cristae formation is a mechanical buckling event controlled by the inner membrane lipidome

Kailash Venkatraman[1], Christopher T. Lee[2*], Guadalupe C. Garcia[3*], Arijit Mahapatra[2*§], Guy Perkins[4], Keun-Young Kim[4], Hilda Amalia Pasolli[5#], Sebastien Phan[4], Jennifer Lippincott-Schwartz[5], Mark Ellisman[4], Padmini Rangamani[2**], and Itay Budin[1,6**]

[1] Department of Chemistry and Biochemistry, University of California San Diego, La Jolla, CA 92093
[2] Department of Mechanical and Aerospace Engineering, University of California San Diego, La Jolla, CA 92093
[3] Computational Neurobiology Laboratory, Salk Institute for Biological Studies, La Jolla CA 92097
[4] National Center for Microscopy and Imaging Research, Center for Research in Biological Systems, University of California San Diego, La Jolla, CA 92093
[5] Howard Hughes Medical Institute, Janelia Research Campus, Ashburn VA 20147
[6] Lead contact.

§ Current affiliation: Applied Physical Sciences, University of North Carolina Chapel Hill, Chapel Hill, NC 27599
# Current affiliation: Electron Microscopy Resource Center, The Rockefeller University, New York, NY 10065

* Equal contributions.
**Contacts: ibudin@ucsd.edu, prangamani@ucsd.edu

Key words: Mitochondria | Lipids | Cristae | Mechanics | Cardiolipin

Abstract

Cristae are high curvature structures in the inner mitochondrial membrane (IMM) that are crucial for ATP production. While cristae-shaping proteins have been defined, analogous mechanisms for lipids have yet to be elucidated. Here we combine experimental lipidome dissection with multi-scale modeling to investigate how lipid interactions dictate IMM morphology and ATP generation. When modulating phospholipid (PL) saturation in engineered yeast strains, we observed a surprisingly abrupt breakpoint in IMM topology driven by a continuous loss of ATP synthase organization at cristae ridges. We found that cardiolipin (CL) specifically buffers the IMM against curvature loss, an effect that is independent of ATP synthase dimerization. To explain this interaction, we developed a continuum model for cristae tubule formation that integrates both lipid and protein-mediated curvatures. The model highlighted a snapthrough instability, which drives IMM collapse upon small changes in membrane properties. It has long been puzzling why loss of CL has only minor phenotype in yeast; we show that CL is in fact essential when cells are grown under natural fermentation conditions that mediate PL saturation.

Introduction

Mitochondria are ubiquitous eukaryotic organelles whose membrane architectures play central roles in both metabolic and non-metabolic functions[1]. The inner mitochondrial membrane (IMM) is the site of the Electron Transport Chain (ETC) and consists of two regions defined by their curvature: the flat inner boundary membrane (IBM), adjacent to the outer mitochondrial membrane (OMM), and cristae membranes (CM), which invaginate into the matrix and are connected to the IBM by crista junctions (CJs)[2,3]. CM structure is dependent on organism, tissue and physiological state[3,4] but is commonly composed of tubular and lamellar membranes[4–74–68]. A clear function of cristae is to effectively increase the surface area for ETC reactions within the membrane. It has also been proposed that cristae invaginations act as a 'proton sink' where protons accumulate and expeditiously flow from the ETC to F_1F_0 adenosine-triphosphate (ATP) synthase[9–11]. Another model is that cristae act as diffusion barriers for metabolites between the intracristal space (ICS) and the intermembrane space (IMS), controlling the flux of ADP/ATP through the adenine nucleotide translocase (ANT)[12–15]. All these potential functions of cristae are dependent on their high intrinsic membrane curvature.

The IMM is shaped by proteins that drive assembly and maintenance of cristae. The molecular determinants of CM are best understood in *Saccharomyces cerevisiae,* where ATP synthases form ribbon-like rows of dimers which induce curvature along tubule and lamellar rims[9,16–18]. Loss of the dimerization subunit *g*, Atp20p, results in monomeric ATP synthases and onion-like mitochondria with flat layers of IMM running parallel with the OMM[19–22]. When reconstituted, ATP synthase dimers spontaneously assemble into rows driven by changes to elastic membrane bending energies[23] and are sufficient to form tubular liposomes[18]. At the CJ, Optic atrophy protein 1 (OPA1)/Mgm1p are dynamin-related GTPases that interact with the mitochondrial contact site and cristae organizing system (MICOS) complex[24–29]. Cells lacking Mgm1 feature a completely flat IMM[30,31], while loss of the major MICOS subunit Mic60p results in elongated cristae sheets that do not contain CJs[22,24].

In addition to its proteinaceous determinants, mitochondrial lipids are hypothesized to also play key roles in shaping cristae structure. The predominant phospholipids (PLs) of the IMM are phosphatidylethanolamine (PE), phosphatidylcholine (PC) and cardiolipin (CL)[32,33]. IMM phospholipids, or their phosphatidylserine (PS) precursors in the case of PE, are imported from the ER at contact sites[34]. A notable exception is CL and its precursor phosphatidylglycerol (PG), which are synthesized in and remain localized to the IMM. Among PLs, CL is unique in featuring four acyl chains whose larger cross sectional area contributes to an overall conical shape[35,36]. CL can be in a dianion or monoanion form[37–39]. While the latter features a larger curvature, it is only present in acidic conditions. In liposomes, CL localizes to regions of high curvature and can drive the pH-dependent formation of invaginations[40–42], which suggests a role in promoting highly curved membrane topologies. The curvature of CL varies in magnitude depending on the local lipid and chemical environments[36,43]. Molecular simulations predict key roles for CL ionization state[44] and binding of counter ions[45] in its curvature. Despite these biophysical data, the fundamental mitochondrial functions of CL are not fully resolved. In the genetic disorder Barth syndrome, loss of the acyl chain remodeler Taffazin causes reduced amounts and altered composition of CL[46,47] leading to abnormal cristae[48], which have also been observed in cell lines lacking CL synthesis[42,49–51]. In yeast, however, loss of cardiolipin synthase (Crd1p) does not render a respiratory or morphological phenotype under regular growth temperatures[52,53]. It thus remains unknown if CL serves a mechanical role in the IMM, or has more organism-specific functions relating to ETC enzymes[54] and their organization[55].

The acyl chain composition of mitochondrial PLs also differs from the rest of the cell[56] and broadly regulates membrane biophysical properties. The IMM is especially enriched in unsaturated and polyunsaturated PLs, which promote membrane fluidity, and lacks sterols and saturated sphingolipids, which promote membrane ordering[57,58]. During synthesis, lipid unsaturation is controlled by the activity of fatty acid desaturases, such as Ole1p in yeast[59,60]. *OLE1* was discovered in genetic screens for both unsaturated fatty acid auxotrophy and mitochondrial distribution and morphology genes (MDM). Mutations in *mdm2* resulted in abnormal mitochondrial morphology and inheritance[61,62] but were later identified as *OLE1* alleles, indicating an unexplained link between desaturase activity and mitochondrial structure. In mammalian cells, addition of exogenous saturated fatty acids (e.g. palmitate) has long been observed to drive mitochondrial abnormality[63–65], but the underlying mechanisms of these perturbations have not been identified. Metabolic diseases including obesity and type-2 diabetes mellitus have been associated with both saturated fat accumulation and mitochondrial stress[66,67]. Saturated PLs could modulate respiration through diffusional effects on electron carriers[68], but these are unlikely to drive large changes in mitochondrial morphology.

Computational modeling can provide a framework to interrogate how changes in lipid composition impact membrane properties and influence cellular structures[69–73]. Molecular dynamic simulations can be used to predict changes to membrane properties as a function of composition[74–76], while continuum modeling can be used to obtain the governing equations for the shape of the membrane given its material properties [77–79]. In the Helfrich-Canham-Evans model[80–82], membranes are treated as a two-dimensional surface with an elastic bending energy given by:

$$E = \int_{\Omega} (\kappa_c (H - C_0)^2 + \kappa_G K) dA \; + \; \lambda dA.$$

where κ_c is the bending modulus of the membrane (stiffness), H is the mean curvature of the structure, C_0 is the net spontaneous curvature across the bilayer, κ_G is the Gaussian modulus, K is the Gaussian curvature, and λ is the membrane tension. The total energy of the membrane (E) is obtained by integrating the energy density of the manifold over the area Ω. When this energy is minimized, the shape of the membrane corresponding to mechanical equilibrium is obtained. Key parameters of this model can be modulated by lipid chemistry. For example, the stiffness (κ_c) of saturated PL bilayers is higher than those with unsaturated (Table S1A, B) and polyunsaturated chains[83,84]. Reconstituted membranes from porcine IMM lipids have been observed to be especially soft (low κ_c)[85]. Curvature induced by differences in lipid abundance or intrinsic spontaneous curvatures (c_0) of lipids across the two leaflets of the bilayer can be modeled as a net membrane spontaneous curvature C_0. PL composition is a major determinant of c_0, which ranges from near zero for cylindrical lipids like PC, to negative values for conical lipids like PE or CL, and positive in the case of lyso-PLs[86]. PL acyl composition also modulates c_0, with more voluminous unsaturated chains favoring negative spontaneous curvatures[87].

Here we combine experimental perturbations with mutli-scale modeling to elucidate new roles for conserved mitochondrial lipids in IMM morphology. We first used genetic manipulation of the desaturase Ole1p to control PL saturation in yeast and observed a surprising lipidic breakpoint, in which the IMM becomes flat and mitochondria lose their ATP synthesis capacity. This transition is controlled by the IMM lipidome in two distinct ways: through modulation of ATP synthase oligomerization by PL saturation and through loss of CL. We develop a mathematical model to explain these effects by considering the energetics of lipid and protein-mediated membrane curvature. We then show CL function is dependent on growth conditions that modulate PL saturation, most notably oxygenation, and that it has an essential role in natural yeast growth environments.

Results

Systematic modulation of the yeast PL double bond profile reveals a critical mitochondrial breakpoint in IMM curvature and ATP generation

Bulk membrane properties are regulated by PL composition, most notably the stoichiometry between saturated and unsaturated acyl chains. To modulate lipid saturation of budding yeast we utilized a library of promoters controlling the expression of Ole1p (Figure 1A). We focused on four strains, saturated fatty acid (SFA) 1-4, which showed a range in lipid saturation (Figure 1A). SFA1 features a wild-type (WT) PL composition while SFA2-4 have consecutively increasing levels of PL acyl chain saturation due to lower levels of *OLE1* expression (Figure S1A). Among PC and PE lipids, WT and SFA1 strains possess predominantly di-unsaturated PLs, while SFA 2,3 and 4 (weaker *OLE1* expression) show an increasing ratio of mono to di-unsaturated species and incorporation of fully saturated PLs (Figure 1A). We observed potentially compensatory adaptations to increasing saturation in whole cell PLs (Figure S1), including a decrease in the PE/PC ratio (Figure S1B), used by several organisms to increase membrane fluidity[88,89], an increase in PI (Figure S1B), and shortening of acyl chains length (Figure S1C), which also occurs during yeast cold adaptation[90].

When handling these strains, we observed that SFA3 and SFA4 cells lost viability in non-fermentable carbon sources (Figure 1B). While SFA1 and SFA2 cells respired at WT-levels, but SFA3/4 showed a reduction and loss of respiratory function (Figure 1C), respectively, indicating that a modest increase in saturation confers a sudden loss in respiratory function. Microscopy of cells expressing a matrix-localized RFP revealed a striking loss in tubular mitochondrial networks and prevalence of aberrant mitochondria in SFA3 cells (Figure 1D, 1E, Figure S2B), while other organelles remained unperturbed (Figure S2A). SFA3 and SFA4 mitochondria also featured gaps in Cox4-GFP, a subunit of cytochrome *c* oxidase in the IMM, as in Δ*atp20* and Δ*mgm1* cells that lack CMs (Figure 1F). Transmission electron microscopy (TEM) analysis of SFA4 cells prepared by high-pressure freeze substitution (HPFS) (Figure 1G, S3A,B) showed mitochondria with flat IMM membranes similar to those previously observed in Δ*atp20* cells[19] or Δ*mgm1* cells[30]. The moderate increase in saturation in SFA2 cells, which does not cause aberrancy independently, also showed epistasis with loss of shaping proteins at both the cristae ridge and rim: Atp20p and Mic60p of the MICOS complex, respectively (Figure S2C, S2D). We thus hypothesized that PL saturation has a specific role in cristae membrane formation.

We next asked how increasing lipid saturation resulted in the aberrant mitochondrial morphologies. We observed that aberrant mitochondria in SFA strains showed elevated membrane potential compared to non-aberrant mitochondria (Figure 1H), as measured by imaging of cells stained with tetramethylrhodamine ethyl ester (TMRE). This phenotype was inconsistent with a loss of proton-pumping reactions in the ETC. It instead suggested an impediment in ATP synthesis itself; TMRE fluorescence of aberrant mitochondria was similar to that when ATP synthase was inhibited by oligomycin in WT cells. We analyzed ATP synthase in isolated mitochondria with blue native PAGE (BN-PAGE) western blotting, which assays both enzyme levels and organization. In mitochondria from SFA strains, increasing saturation did not reduce ATP synthase levels, but instead altered its organization. SFA1 mitochondria show WT-levels of ATP synthase dimers and oligomers, while in SFA2 oligomers are lost, and SFA3

and SFA4 contain predominantly contained monomeric ATP synthases, similar similar to Δ*atp20* (Figure 1I). Thus, unsaturated lipid metabolism modulates the ATP synthase oligomerization.

Modeling of transport processes in aberrant mitochondria suggest a mechanism for loss of ATP generation

The loss of ATP synthase oligomerization in more saturated lipidomes provides one possible mechanism for loss of CM morphology, but does not fully explain loss of respiration given that monomeric ATP synthases largely retain ATPase activity[19,20]. To further investigate the function of IMM morphology, we sought to characterize the morphological and surface area changes to the IMM of SFA strains (Figure 2). For this, 3D reconstructions generated from multi-tilt TEM were meshed using the GAMer2 platform[7,91,92] (Figure S3D) and local membrane curvature was computed across their surfaces. SFA2 tomograms displayed tubular CMs in the IMM similar to WT cells; these invaginated regions contain regions of high mean and deviatoric curvatures (Figure 2A, 2C-D). In contrast, the two types of aberrant morphologies in SFA4 cells showed a loss of high (>25 μm^{-1}) mean and deviatoric curvatures (Figure 2B, 2C-D). Flat (Δ*mgm1*-like) IMM were defined by an identical curvature profile as the OMM and a reduced surface area:volume (SA:V) ratio (Figure 2E). Onion-like mitochondria with multiple IMM layers (Δ*atp20*-like) possessed an increased SA:V ratio, but still lacked any of the high curvature regimes of the CMs (Figure 2E, 2C-D). Wide-field TEM showed that mitochondria with multiple IMMs made up at least 40% of SFA4 mitochondria (Figure S3A). Tomography of onion mitochondria revealed that the membrane layers showed connection vertices (Figure S3C), suggesting a continuous IMM. We also noted a distinct alternating shading pattern of high contrast matrix regions alternating with low contrast IMS layers (Figure S3B), which were previously observed in Δ*atp20* cells[19]. These two features are consistent with a model in which mitochondria with multiple layers could arise from repeated low curvature buddings from a continuous, single IMM (Figure S3C).

While flat IMMs show a reduced surface area for ETC reactions compared to CM-containing ones, onion-like IMMs with multiple layers instead show a high surface area (Figure 2E). Previous modeling studies have shown that surface-to-volume ratio is an important determinant of flux of molecules between different compartments[93–95]. We hypothesized that multiple concentric layers would likely impede transport of ATP out of, and ADP into, the mitochondria of SFA3/SFA4 and Δ*atp20* cells. To explore this hypothesis, we employed an MCell-based reaction-diffusion simulation pipeline for modeling ATP generation using EM-derived morphologies[96–98]. These simulations showed that mitochondria with multiple IMM layers cause lower ATP generation when cytosolic ADP concentration was kept constant (Figure 2F, 2G, 2H). We also observed that predicted ATP production was inhibited by depletion of ADP as a substrate in the inner layers of the onion-like IMM, highlighting that ATP/ADP exchange by ANT could be limiting for high surface area IMM morphologies with low membrane curvature (Figure 2I). These simulations suggest that efficient substrate transport could be dependent on the architecture of CMs in addition to IMM surface area.

Lipid saturation modulates membrane mechanical properties which are buffered by mitochondrial-specific head group changes

To define the lipid stoichiometry that drives CM loss, we analyzed biochemically isolated mitochondria from SFA strains. As in the whole cell lipidome, increasing Ole1p activity in SFA strains increased mitochondria PL saturation, but few fully saturated species were observed. The lipidome of isolated inner membranes was similar to that of intact mitochondria from the same sample, with the notable exception of CL levels (Figure S1F). The lipidic breakpoint in

SFA3 cells corresponded to changes in the double bond distribution from predominantly di-unsaturated to monounsaturated PLs, e.g. PE-16:1/18:1 to PE-16:0/16:1 (Figure 3A, 3B), a surprisingly modest shift given the magnitude of the morphological change.

To explore the effects of this change in acyl chains on membrane properties, we set up simulations of lipid bilayers mimicking the mitochondrial composition of SFA strains. We employed coarse-grained molecular dynamics (CG-MD) simulations, which forego atomistic detail in favor of enabling improved sampling of complex mixtures and the modeling of larger domains and shape transformations[99,100]. To test whether the CG-MD simulations capture known mechanical properties of saturated PLs, we first simulated simplified mixtures of inner mitochondrial lipidomes (50:30:20 PC:PE:CL) containing either monounsaturated or diunsaturated PC & PE. Simulations of large membranes (~40 nm x 40 nm, 5000 lipids) were conducted and the thermally induced height undulations were analyzed to derive the bending stiffness (κ_c) of each membrane composition. In parallel, small membranes (~15 nm x 15 nm, 700 lipids) of identical compositions were used to compute stress (lateral pressure) profiles, whose first moment is equal to the product of κ_c and the monolayer spontaneous curvature, c_0. Using κ_c values derived from the large systems, c_0 values can thus be extracted. Shifting from diunsaturated to monounsaturated PLs led to a ~30% increase in stiffness, κ_c, (Figure 3C), consistent with previous experimental measurements in monocomponent liposomes (Table S1A-B). Similarly, monounsaturated mixtures showed a ~25% increase in c_0, which was consistent with previous measurements in monocomponent mixtures measured by small angle x-ray scattering (Table S1C). We concluded that CG-MD using the Martini 2 force field is capable of reproducing the expected changes to mechanical properties modulated by PL lipid saturation. We thus proceeded to more complex mixtures derived from mitochondrial lipidomes.

In lipidomics of SFA strains, we observed a mitochondrial-specific change in head group composition: PE levels increased with increasing saturation at the expense of PC, resulting in an increase in the PE/PC ratio (Figure 3D, Figure S1E). In contrast, the PE/PC ratio decreased in the corresponding whole cell lipidome (Figure 3D, Figure S1B). Because PE has a higher melting temperature than PC[88], its increase in SFA strains argues against a fluidity-specific stress of saturation on the mitochondria. Instead, the high negative spontaneous curvature of PE suggested an adaptation to membrane spontaneous curvature itself. To understand the biophysical basis for this adaptation, we employed the CG-MD workflow described above using more complex lipid mixtures that mimic the changes in head-group composition in SFA strains (Figure 3E). In these systems, shifting from the WT mitochondrial lipidomes to those of the SFA3 mitochondria resulted in only a modest increase in stiffness (κ_c) and no change to the magnitude of c_0, despite the increase in PL saturation (Figure 3F). These findings suggested that mitochondrial specific adaptations in SFA strains act to buffer membrane mechanical properties relevant to curvature generation.

Beyond changes in the PE/PC ratio, our membrane simulations highlighted the key role of CL in dictating properties relevant to curvature generation. Replacement of CL with its precursor lipid PG resulted in an overall stiffening of simulated IMMs (Figure S4D-E) and loss of spontaneous curvature. Switching CL from the dianion form predominant at neutral pH to the monoanion form had the opposite effect, dramatically softening the bilayer and increasing spontaneous curvature (Figure S4D-E). In simulations without CL, the increase in PE in SFA strains could only partially compensate for curvature lost when CL was removed (Figure S4F). CL preferentially clustered with PE lipids in the simulated bilayers (Figure 3G), highlighting how conical lipids sort together in areas of high curvature[101]. This association was maintained in SFA lipidomes, though the extent of CL-PE association was reduced in the saturated SFA3 bilayers (Figure 3G).

An epistasis between PL saturation and CL abundance underlies IMM structure

The observation that mitochondria in SFA2 cells responded to increased PL saturation by increasing the abundance of high-curvature PE and CL lipids compared to WT (Figure S1D) led us to consider the interplay of lipid curvature and saturation. While PL saturation modulates intrinsic lipid curvature (c_0) (Table S1C), there is no evidence that acyl chain composition differs across the two leaflets of the IMM, which would be needed to generate net membrane curvature (C_0). We instead hypothesized that the effects of CL on predicted membrane curvature described above and the established asymmetric localization of CL in the IMM[102] could provide membrane curvature independent of cristae shaping proteins, such as ATP synthase dimers. To explore this possibility, we tested out compositions based on previously measured asymmetries of CL in the yeast IMM. The simulations predicted that enrichment of CL in the IMM outer leaflet increased c_0 and reduced κ_c (Figure S4G). Based on values for the former, we estimated that CL asymmetry could contribute at least a -0.05 nm^{-1} net bilayer curvature (C_0) (Figure S4G).

We next asked whether IMM curvature imparted by CL could compensate for loss of curvature imparted by lipid saturation and loss of ATP synthase oligomerization. For this, we evaluated how loss of Crd1p, which catalyzes the condensation of PG with a cytidine diphosphate diacylglycerol (CDP-DAG) molecule to form CL, affects mitochondrial morphology in SFA1-4 strains (Figure 4A). CL was absent in Δ*crd1* strains in isolated mitochondria, which also showed a substantial increase in PG (Fig 4A). We also confirmed that loss of CL in SFA strains did not result in modification of PL acyl chain saturation (Figure 4A). As previously observed[52], Δ*crd1* cells did not show defects in mitochondrial morphology or cellular respiration in WT (*CRD1*) or SFA1 backgrounds (Figure S6A-B). However, in the SFA2 background, which shows increased saturation and reduced ATP synthase oligomerization but normal mitochondrial morphology, loss of CL had a dramatic phenotype (Figure 4B-E). SFA2Δ*crd1* exhibited aberrant mitochondria (Figure 4C) that lack cristae membranes (Figure 4D-E) as previously observed in SFA3/SFA4. Respirometry measurements confirmed these results: Δ*crd1* and SFA1Δ*crd1* strains were able to respire at the same rate as *CRD1* cells, SFA2Δ*crd1* exhibited a perturbed oxygen consumption rate (Figure 4B). Loss of morphology and respiration in SFA2Δ*crd1* was completely rescued by supplementation with oleic acid, demonstrating that Δ*crd1* has a specific interaction with PL saturation (Figure S6C).

While loss of CL modulated CM formation under increased PL saturation, it did so independently of ATP synthase dimerization. Δ*crd1* cells showed no defect in ATP synthase oligomerization compared to *CRD1* cells, while SFA2Δ*crd1* cells maintained an identical level of oligomerization found in SFA2 cells (Figure 4F). However, loss of CL still showed a strong epistasis with the saturation induced loss of ATP synthase oligomerization in SFA2 cells, as well as with complete loss of dimerization in Δ*atp20* cells (Figure S6D). Thus, CL acts orthogonally to PL saturation and ATP synthase oligomerization to modulate IMM morphology, but only under conditions where the latter is reduced compared to WT cells grown in laboratory conditions.

Modeling predicts compensatory roles for lipid and protein-encoded curvature in shaping cristae tubule formation

To understand the interaction between CL, which contributes to net membrane spontaneous curvature, and ATP synthase oligomers, whose induced curvature is localized specifically at cristae ridges, we employed continuum modeling framework based on previous efforts to model membrane tubule formation[73,103–105]. We modeled the simplest CM structure — cristae tubules — as axisymmetric tubes that bud from a flat membrane (Figure 5A). We added a pre-defined coat area of ATP synthase oligomers that contribute an anisotropic curvature (D_0). An isotropic

membrane curvature (C_0) was then applied across the entire membrane to model the effects of asymmetrically localized CL. In simulations, we varied the magnitude of D_0 and C_0 based on data from simulations of curvature induced by ATP synthase dimers[23] and CL effects on mitochondrial membrane compositions estimated by simulations of outer and inner IMM leaflets (Figure S4G). In both cases, the approximate ranges were set to 0 to 0.035 nm^{-1}. The stiffness of the membrane was also varied across biologically reasonable values (10-20 k_BT) and the membrane tension was set at 0.01 pN/nm[104]. Finally, to incorporate the stresses due to the proposed roles of the MICOS complex and Mgm1 at the CJs, we used a localized collar force density of 8 pN/nm around the base of the tubule neck. Additional details of the governing equations and parameters of the model can be found in the Supplementary Text.

We observed that the combination of isotropic and anisotropic spontaneous curvatures is sufficient to deform the membrane into different shapes reminiscent of flat membranes, buds that could be relevant for onion-like IMM formation, and CM-like tubules (Figure 5B). High values of anisotropic spontaneous curvature (Figure 5B, third column) promoted the formation of long tubular structures for all values of isotropic spontaneous curvatures and bending moduli, and did so independently of the presence of the collar force (Figure S5). Tubule length and diameter were generally consistent with that of CMs in cells (Figure 5B). Low values of anisotropic curvature (e.g. no ATP synthase oligomerization), did not allow for tubule formation and instead led to flat or bud-like structures (Figure 5B, i-iii). The latter was observed even when isotropic spontaneous curvature, potentially encoded by CL, remained high. For intermediate values of anisotropic curvature, which could approximate the state in SFA2 cells that show partial loss ATP synthase oligomerization, higher values of isotropic curvature resulted in shapes that still resembled cristae (Figure 5B, ii and v), while lower values of isotropic curvature resulted in shallow invaginations. From these simulations, we predicted that a combination of either high isotropic or anisotropic curvatures are sufficient for forming cristae-like structures relevant to observed phenotypes in cells. Specifically, the dependency of tubule formation on isotropic spontaneous curvature when anisotropic spontaneous curvature is partially lost could explain the interaction observed between CL and PL saturation. We note that similar calculations in the absence of the collar force (Figure S5), show bud-like and tubular structures with a wider neck, consistent with the model that local forces exerted by the MICOS and Mgm1p shape CJs[22,28,106,107].

Further investigation into the parameter space for cristae-like tubular structures revealed a transition from the short U-shaped invaginations to the long tubular structures in an abrupt manner (Figure 5Ci). This transition was observed as the anisotropic curvature (e.g. via ATP synthase oligomerization) increased for a fixed value of isotropic curvature (Figure 5Cii) or as the isotropic curvature (e.g. via CL-encoded membrane spontaneous) was increased for a fixed value of anisotropic curvature (Figure 5Cii) for the different values of bending moduli (see also Figure S5 for additional simulations). This sudden change in length is characterized by a snapthrough transition, where a small amount of thermodynamic work done on the system, by changing either material properties or curvatures induced, results in a change in the minimal energy state of the system where a tube-like shape is a low energy configuration[103,104,108,109]. We observed that the curvature values at which this transition occurs was modulated by the presence of a collar force at the tubular neck, suggesting that mechanics could underlie the functional interactions observed between Mic60p at the CJ and PL saturation (Figure S2C, Figure S5). These simulations thus predict that the formation of cristae-like structures in mitochondrial membranes can result from mechanical instabilities and that these instabilities are governed by the composition and mechanical properties of the IMM.

CL is an essential mitochondrial lipid in natural yeast environments

Given the role of CL in cristae morphology of more saturated IMMs and the conservation of CL synthesis among eukaryotes[110], we considered the physiological function for CL in yeast. The lack of phenotype for Δ*crd1* strains under standard laboratory growth conditions has long been perplexing, given the demonstrated importance of CL for mitochondrial function in other organisms[111]. However, natural yeast environments, such as rotting fruits or fermentation tanks, differ starkly from laboratory conditions, especially with regards to the availability of molecular oxygen. Like other lipid desaturases, Ole1p consumes oxygen as an electron acceptor, which binds to a low-affinity (K_M ~60 μM) di-iron site[112]; thus the enzyme's activity is sensitive to environmental oxygenation[113,114]. Cells grown in microaerobic fermenters show a lower level of di-unsaturated phospholipids than those grown under highly aerated conditions (low volume shake flask); their lipidomes are an intermediate between that of aerated SFA2 and SFA3 cells (Figure S6E). *CRD1* cells grown under microaerobic conditions also showed similar whole cell headgroup compensations (a decrease in the PE/PC ratio) as SFA2 strains (Figure S6F). We hypothesized that in these less aerated environments, CL metabolism could have evolved to support an essential mechanical function.

To test the role of oxygenation on CL function, we grew *CRD1* and Δ*crd1* yeast strains in microaerobic chambers, comparing their lipidomes and mitochondrial morphologies to those grown in highly aerated shake flasks (Figure 6A). Under limited oxygenation, *CRD1* cells increased the abundance of CL twofold compared to highly aerated conditions (Figure 6B), counter to the canonical role of CL in respiratory metabolism. Both *CRD1* and Δ*crd1* cells showed increased levels of PL saturation in the total PL pool (Figure 6C), and in major Pl classes PC and PE (Figure S6F), under microaerobic conditions. Importantly, loss of CL did not have an effect on the levels of acyl chain saturation (Figure 6C). After microaerobic growth, yeast containing CL still presented tubular mitochondrial morphology, but Δ*crd1* cells displayed a stark increase in aberrant mitochondrial morphologies (Figure 6D, 6E). We also observed that Δ*crd1* cells showed increased abundance of PE lipids under microaerobic conditions, potentially as a curvature compensation for lack of CL in the cell (Figure S6F). Ultrastructural analysis of IMM structure revealed that *CRD1* cells grown under microaerobic conditions displayed tubular cristae morphologies while Δ*crd1* cells displayed a mixture of flat and onion-like IMM structures (Figure 6F). CL is thus required for mitochondrial biogenesis during yeast fermentation, but not in the highly oxygenated laboratory conditions used by most mitochondrial research.

Discussion

While a large body of research has identified specific proteins that shape the IMM, analogous roles for lipids have been less defined. Here we explored an initial observation that small changes to the unsaturation of PL acyl chains in yeast specifically causes a loss of CMs, similar to what has been observed upon loss of cristae shaping proteins. We found that di-unsaturated PLs promotes ATP synthase oligomerization, which is progressively lost when the activity of the lipid desaturase Ole1p decreases. We then explored a key interaction between 1) the curvature at cristae ridges induced by ATP synthase oligomerization and modulated by PL saturation and 2) lipid-encoded curvature across the IMM, which is promoted by conical lipids like CL. Both of these define whether the IMM exists in a high or low curvature state, which in turns controls ATP production.

We propose that intrinsic membrane curvature can be generated both by proteins and by asymmetric distributions of lipids across the bilayer, which contributes net spontaneous curvature between the two leaflets. For CL, there are at least three potential sources by which net curvature is generated. First, extensive measurements of compositional asymmetry of CL have been performed in yeast using nonyl acridine orange, which preferentially interacts with CL on the outer (IMS-facing) leaflet at low concentrations[102,115]. These suggest that the yeast IMM features up to 2-fold more CL in the outer leaflet, which would optimize its negative curvature at cristae ridges. Second, the differences in local pH between the matrix and intermembrane space could favor the monoanion species in the leaflet facing the latter, which would also promote negative curvature at the cristae ridge. Finally, CL and other conical lipids would segregate into deformed membrane regions, further promoting curvature. Such a phenomenon has been observed experimentally when CL localized to thin, high curvature tubules that have been pulled from large, low curvature vesicles[36]. In simulations, this effect is apparent in localized CL concentrations in thermal fluctuations (Figure 3G) and those induced by compression[44,116]. In the IMM, it is likely that local deformations induced by ATP synthase[18] cause the local concentration of conical lipids (e.g. CL and di-unsaturated PE), which further act to deform the IMM. The action of membrane shaping lipids and proteins are therefore likely to be intrinsically linked.

In response to perturbations, we observed mitochondrial-specific lipidomes that are consistent with curvature-based effects of both PL saturation and CL. Increasing saturation through lowering of *OLE1* expression in SFA strains causes an increase of PC in cells, which increases fluidity compared to PE and can thus be understood in a homeoviscous adaptation framework. However, in the mitochondria, increased saturation has the opposite effect, increasing PE levels to counteract the loss in lipid spontaneous curvature. Analogously, under microaerobic conditions, CL levels increase compared to highly aerobic cells, despite limited usage of the ETC for energy production in the former. Cells rely on mitochondria for other metabolic tasks, such as amino acid and cofactor biosynthesis[117], and so maintenance of IMM structure is still required under fermentation conditions. Additional CL could supplement the loss of di-unsaturated PLs due to limited Ole1p activity. We observe a similar change in the CL content of SFA2 mitochondria. Though SFA3 mitochondria show a loss of CL, this corresponds to dramatic increase in saturation specifically in CL, which could limit spontaneous curvature and promote its degradation[118]. These examples of mitochondrial lipid adaptation suggest unidentified mechanisms in the IMM to sense and respond to changes in membrane curvature.

The interplay with PL saturation provides a biophysical rationale for long-standing questions regarding the cellular roles of CL. Despite its ubiquity among eukaryotes, the reported functions of CL have differed strikingly across experimental systems. While loss of CL is lethal in mice[52,54,119] and drives CM loss in mammalian cell lines[120], it has only minor phenotypes in yeast

grown under common laboratory conditions. In *Drosophila*, loss of CL reduces the density of ETC components in the IMM and thus modulates respiration[54], but also does not cause loss of CMs. We propose that the mechanical functions of CL function are dependent on the surrounding lipid environment in the IMM, which can change depending on growth conditions. Under yeast growth conditions that cause higher PL saturation, we find that CL is essential for CM formation. These are likely to better mimic the oxygenation of natural yeast environments, such as rotting fruits. Yeast grown under highly aerated laboratory conditions (shake flasks or culture tubes shaking at >100 rpm) instead show an unusually high level of di-unsaturated PLs. The acyl chain composition of PE and PC in mammalian cell lines and tissues, where CL is essential, more closely resemble those of microaerobically grown yeast or the aerobically grown SFA2 strain (Figure S1G). In the case of *Drosophila*, an elevated PE/PC ratio[121,122] might also compensate for the loss of CL. It is notable that these model systems are being widely utilized to study the mechanisms underlying Barth syndrome, a disease caused by altered CL metabolism. In humans, lipid saturation is highly influenced by diet and other metabolic states[123] and so these could be relevant to the pathology of CL loss. Global analysis and modeling of mitochondrial lipidomes could be required to understand the function of CL in different organisms and metabolic conditions.

To understand how membrane curvature generated by CL can act independently of ATP synthase dimerization, we carried out mechanical modeling of tubules as the simplest CM structure. Modeling predicted that intermediate levels of anisotropic curvature at the tubule ridge can be compensated by high isotropic curvature encoded by the lipidome, which is consistent with observations of how CL modulates IMM structure in SFA2 vs. SFA2Δ*crd1* cells. An additional motivation for employing continuum models for biological structures is to identify the physical principles that could underlie their formation in cells. CM formation in yeast is an example of a bimodal process: cells either show high curvature tubules or flat structures due to both lipidome changes or loss of cristae-shaping proteins. Our simulations suggest that tubule formation is defined by a snap-through instability, in which a system can shift between two morphological states via modest perturbations in its properties or forces applied. Such buckling events are intrinsic to the Helfrich model depending on choice of coordinates[124,125] and have previously been shown for other curved structures, such as buds in endocytosis[104,108]. They are thus likely to apply for other CM structures. The IMM is just one example of a highly curved membrane in cells; others include narrow tubules in the peripheral ER[126] and rims of Golgi cisternae[127]. A common feature across these organelles is that regions of very high curvature are present alongside those with low curvatures[7,128,129]. While relevant curvature-inducing proteins have been identified in these structures, how bimodal distributions of curvature are stabilized within the same continuous lipid membrane is less clear. Membrane compositions that border snapthrough instabilities could provide a mechanism for this arrangement.

An outstanding question of this work is how specific lipid perturbations modulate the dimerization and higher order organization of ATP synthases. PL saturation, which influences both membrane stiffness and curvature, reduces ATP synthase oligomerization in cells. Among membrane protein dimers, the yeast ER sensors Mga2/Spt23 show a similar dimer to monomer transition when their host membrane shifts di-unsaturated to mono-unsaturated PLs[130,131]. While Mga2/Spt23 are small, single pass transmembrane proteins, the CLC Cl^-/H^+ antiporter dimer has a similar buried surface area as ATP synthase (~2400 $Å^2$) and a modest dimerization free energy (19 k_BT[132]) that is also highly sensitive to its lipidic environment[133]. In CLC, short chain PLs, which notably accumulate in more saturated lipidomes, have been shown to stabilize the monomer conformation and through this mechanism weaken its dimerization. Unlike CLC, dimerization of ATP synthase is associated with an extreme local membrane deformation (a ~90° bend in *S. cerevisiae*[134]). An alternative hypothesis is that the changes in mechanical

properties encoded by PL saturation, especially stiffness, alters the energetics of the local membrane deformation, reducing the dimer:monomer equilibrium by increasing the elastic cost of this deformation. Although adaptive changes in the mitochondrial lipidome could buffer against membrane stiffness (Figure 3D), they are likely to do so incompletely in ways that are not captured by our simplified MD simulations. Distinguishing between these models will require future experiments and modeling, which would be aided by structures of monomeric ATP synthases with fully resolved dimerization subunits.

During the evolution of eukaryotic cells, the machinery for ATP generation in the ETC adopted a secondary function in the shaping of the IMM. The emergence of ATP synthase dimers and other cristae-shaping protein complexes occurred alongside a specialization in the inner membrane lipidome, including the proliferation of CL from the proteobacterial inner membrane[135,136]. Among extant eukaryotes, ATP synthase organization varies widely; for example, in mammalian mitochondria ATP synthases range from primarily monomeric[137] to mixtures of monomers and dimers[138]. It is notable that CL is essential for proper IMM structure in these systems, unlike in aerobic yeast in which dimers are predominant. The composition of other cristae-shaping proteins, such as the MICOS complex[139], also differ across eukaryotes, despite the ubiquity of CMs in mitochondria. Such variability in IMM shaping proteins could have necessitated the utilization of alternative forms of curvature generation encoded by the mitochondrial lipidome.

Acknowledgments

José Faraldo-Gómez, Edward Lyman, and Nicolas-Frédéric Lipp provided helpful discussions. Daniel Degreif and Sterling Ramsey assisted in strain development. Alexander Tzagoloff, Leticia Franco, and Mário Barros supplied reagents. The National Institutes of Health (R35-GM142960 to I.B, R01AG065549, R24GM137200 and U24NS120055 to M.H.E.), the Office of Naval Research (ONR N00014-20-1-2469 to P.R.), the National Science Foundation (DBI-2014862 to M.H.E), the Department of Energy (DE-SC0022954 to I.B.) and the Moore–Simons Project on the Origin of the Eukaryotic Cell (GBMF-9734 to I.B., P.R., and M.H.E.) provided financial support. K.V. was supported by the NIH Molecular Biophysics Training Grant (T32-GM008326C). C.L. was supported by a Kavli Institute for Brain and Mind Postdoctoral Fellowship. Howard Hughes Medical Institute supported initial project conception through the Janelia Visiting Scientist Program. Molecular dynamics simulations were run on hardware hosted by the Triton Shared Computing Cluster.

Author Contributions

K.V. and I.B. designed and carried out the experiments. C.L., G.C.G., A.M., and P.R. designed and carried out the simulations. G.P., K-Y. K., H.A.P., S.P., and M.H.E. carried out electron microscopy. I.B and P.R. supervised the work. All authors contributed to data analysis and writing of the manuscript.

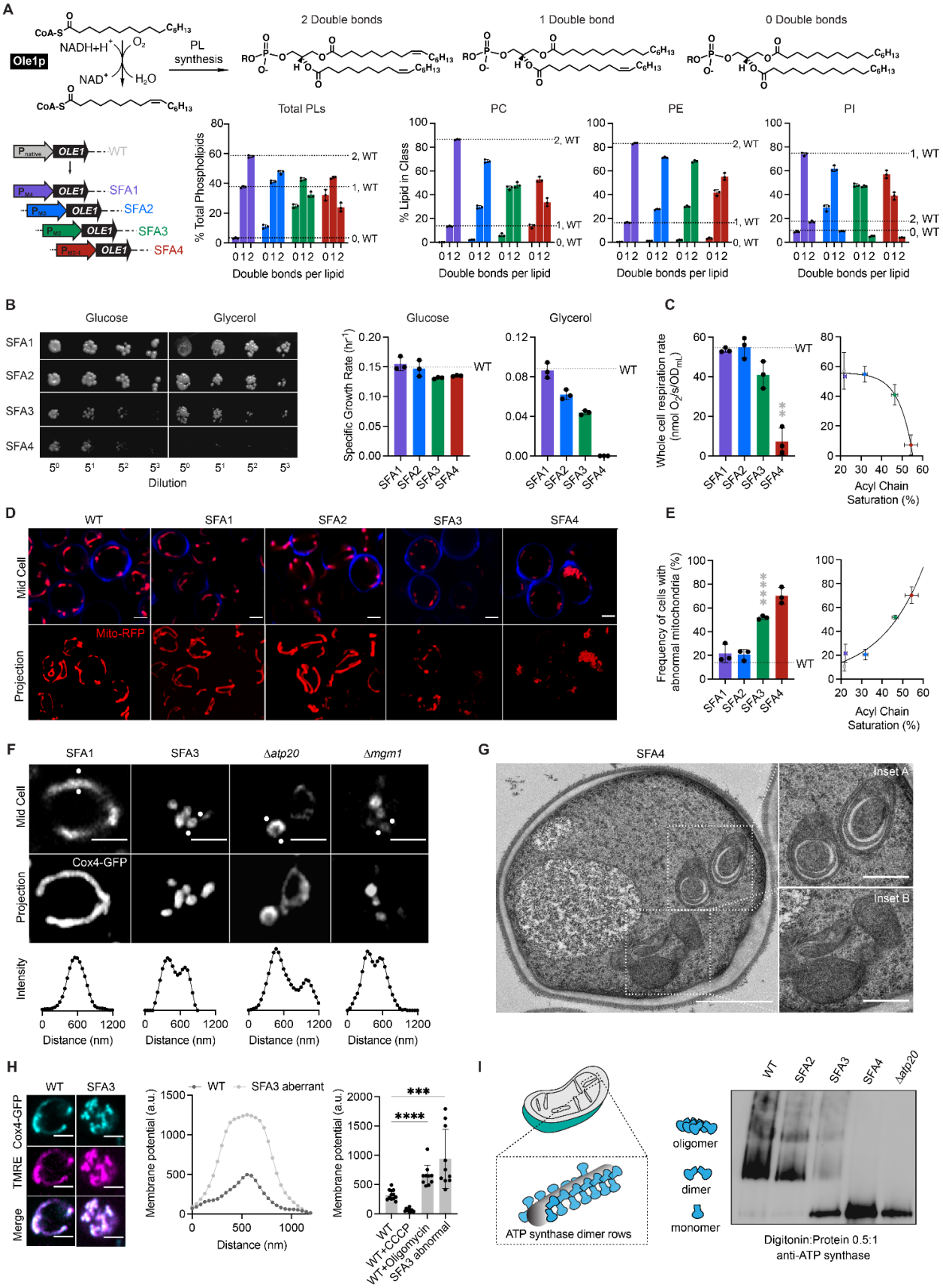

Figure 1: Modulation of *OLE1* expression results in a critical level of PL saturation driving loss of ATP generation and mitochondrial morphology.
(A) The yeast desaturase, Ole1p, is an oxygen-dependent enzyme that introduces *cis* double bonds at the C9 position (top left). SFA strains were generated via promoter substitution, resulting in progressively decreasing levels of *OLE1* expression (bottom left). Lipidomics analysis showing double bond distributions of the total PL pool as well as of individual PLs within SFA strains; the wild-type distribution is depicted with dotted lines. Error bars indicate SD from biological replicates n=3.
(B) SFA4 cells lose viability under respiratory conditions. Shown are serial dilutions of yeast cells plated on media containing fermentable (glucose) and non-fermentable (glycerol) carbon sources and specific growth rates for each in liquid cultures. Error bars indicate SD from n=3 independent cultures.
(C) (Left) SFA3 and SFA4 cells show a drop in whole cell respiration, measured using a Clark electrode. Error bars indicate SD from n=3 independent cultures. **p=0.004, unpaired two-tailed t-test of SFA4 compared against wild-type. (Right) Scatter plot depicting a fitted single exponential (R^2 =0.99) for the decrease in respiration as a function of acyl chain saturation.
(D) SFA3 and SFA4 cells lose tubular mitochondrial morphology. Shown are representative Airyscan confocal micrographs of yeast expressing matrix-localized RFP (mts-RFP). Cells were stained with cell wall-binding calcofluor white (blue) for clarity. Scale bars, 2 μm.
(E) Mitochondrial morphology changes between SFA2 and SFA3 strains, as assayed by confocal microscopy of cells harboring an mts-RFP plasmid. N>50 cells were counted in biological triplicate in each condition. Error bars indicate SD from n=3 independent cultures. ****p < 0.0001, unpaired two-tailed t-test of SFA3 compared against wild-type. (Right) Scatter plot depicting a fitted single exponential (R^2 =0.97) for the increase in frequency of abnormal mitochondria as a function of acyl chain saturation.
(F) Airyscan confocal micrographs of yeast expressing IMM protein Cox4-GFP showing hollow mitochondria in SFA3 cells, as is also observed in mutants of CM shaping proteins. Scale bars, 2 μm. Profiling analysis (below) depicts fluorescence intensity across the indicated mitochondria; two peaks indicate a lack of fenestrated IMM.
(G) Thin section TEM micrographs of high-pressure frozen (HPF) SFA4 yeast showing the appearance of an onion-like (Inset A) IMM and total loss of CM (Inset B). Scale bars, 1 μm (full image), 400 nm (insets A and B).
(H) Abnormal mitochondria show an increase in membrane potential, consistent with loss of ATP synthase, but not ETC, activity. (Left) Representative micrographs are shown of individual cells expressing Cox4-GFP and stained with TMRE. (Center) Example membrane potential plots showing an example of an abnormal SFA3 cell with higher TMRE intensity compared to WT. (Right) Quantification of TMRE peak intensities from N>10 cells per condition showing a higher membrane potential in aberrant mitochondria, as well as those where ATP synthase is inhibited by oligomycin (5 μM), and lower potential in cells treated with the uncoupler CCCP (20 μM). Scale bars, 2 μm. ***p<0.0005, ****p<0.0001 unpaired two-tailed t-test of SFA3 aberrant and WT+oligomycin compared against WT.
(I) ATP synthase oligomerization is lost with increasing PL saturation. SFA2 mitochondria lose higher order oligomers observed in WT cells, while SFA3 and SFA4 mitochondria possess predominantly monomeric ATP synthase, similar to Δ*atp20* cells. Shown are BN-PAGE western blots of digitonin-solubilized purified mitochondria. 2500 pmol of mitochondrial lipid was loaded per well.

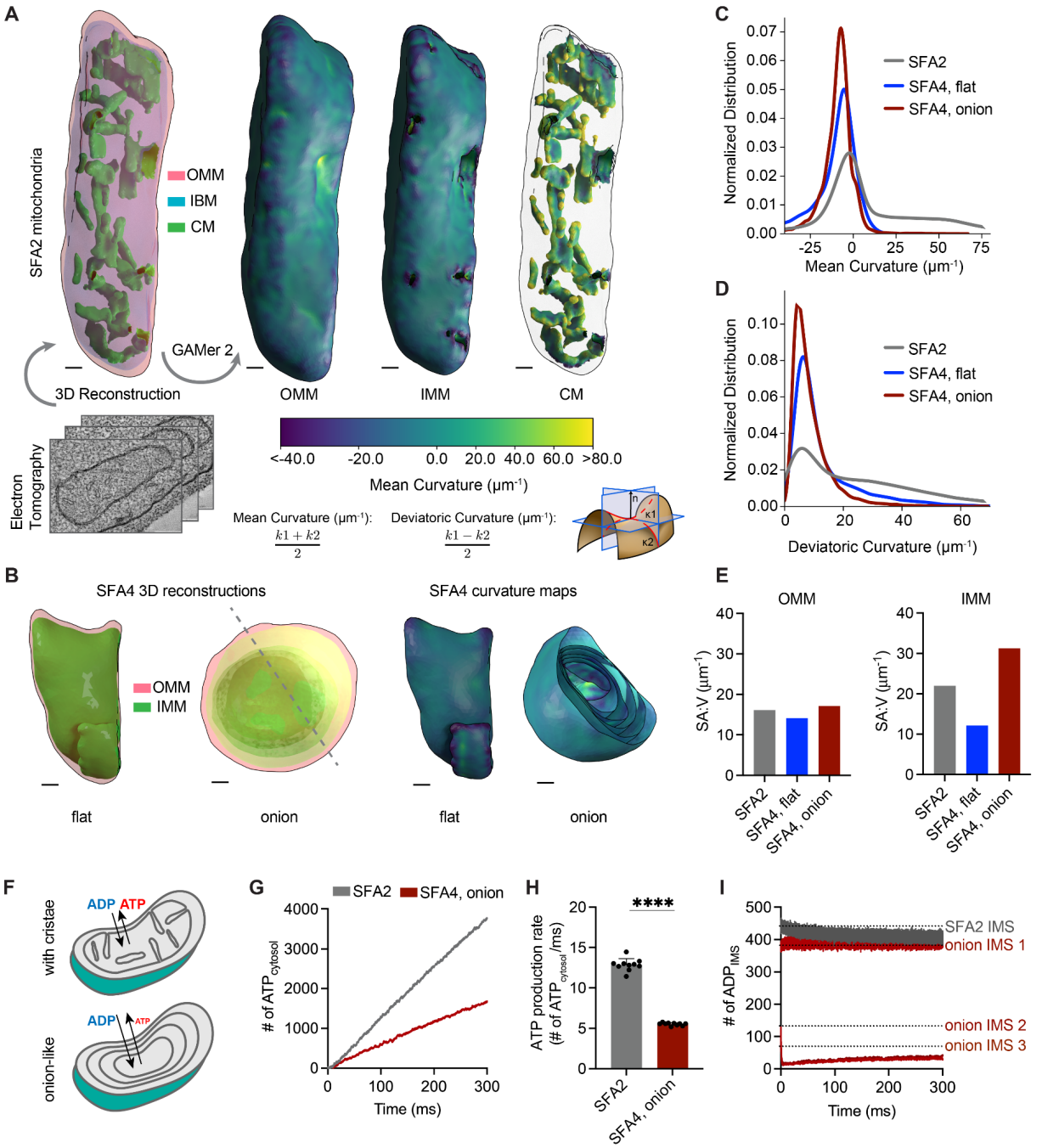

Figure 2: PL saturation shifts the IMM to a regime of low membrane curvature, which reduces IMM surface area and modeled transport rates needed for ATP generation.

(A) 3D reconstruction of mitochondrial membrane topology and quantification of curvature using the GAMer 2 pipeline. Shown are electron tomograms of mitochondria from SFA2 cells, which show regular, tubular CM. CM are highlighted alongside the OMM and the inner boundary membrane (IBM) in the 3D reconstruction. (Right) Maps of mean curvature of OMM, IMM and CM computed using GAMer2. Scale bars, 50 nm.

(B) 3D reconstructions of SFA4 mitochondria showing flat (Δ*mgm1*-like) and onion (Δ*atp20*-like) abnormal morphologies. Also shown are the maps of mean curvature showing the IMM of these abnormal mitochondria, using the same color scale as in A. The onion-like IMM is sliced at an angle to illustrate the many layers; each layer is spherical in nature. Scale bars, 50 nm.

(C) Histograms of mean curvature distributions of inner membranes generated from SFA2 and SFA4 reconstructions, highlighting that high mean curvature areas in SFA2 IMM are lost in SFA4 cells.
(D) Histograms of deviatoric curvature distributions of inner membranes generated from SFA2 and SFA4 reconstructions, which are mechanical corollaries to curvature induced by ATP synthase dimerization, highlight that high deviatoric curvature areas in SFA2 IMM are lost in SFA4 cells.
(E) The IMMs of onion mitochondria show increased surface area:volume (SA:V) ratio compared to SFA2 while flat mitochondria show a decrease in the surface area:volume without major changes to the OMM.
(F) Schematic of ATP production in mitochondria containing normal CMs and those showing a multi-layer, online-like IMM, highlighting how multiple membrane layers could impede in trafficking of ADP and ATP.
(G) Modeled cytosolic ATP generation from mitochondria with a CM-containing morphology (taken from SFA2 tomogram) vs. an onion-like (taken from SFA4 tomogram) IMM. ATP generated in the cytosol in each condition is an average from 10 simulations. Details of the model equations and simulations are provided in the Supplementary Text.
(H) Comparison of cytosolic ATP generation rates derived from multiple Monte Carlo simulations shown in G. 10 simulations were run for each morphology. Error bars indicate SD; ****$p<0.0001$, unpaired two-tailed t-test.
(I) Modeled substrate depletion in onion-like mitochondria. In the CM-containing mitochondrion, the ADP level in the IMS remains constant at ~440 ADP throughout the 300 ms simulation. In the onion-like SFA4 mitochondrion, ADP remains constant only in the first IMS layer and is rapidly depleted in layers 2 and 3, indicating that the multi-layer structure could be limiting for ATP/ADP trafficking. Dotted lines represent initial values of ADP in each IMS layer.

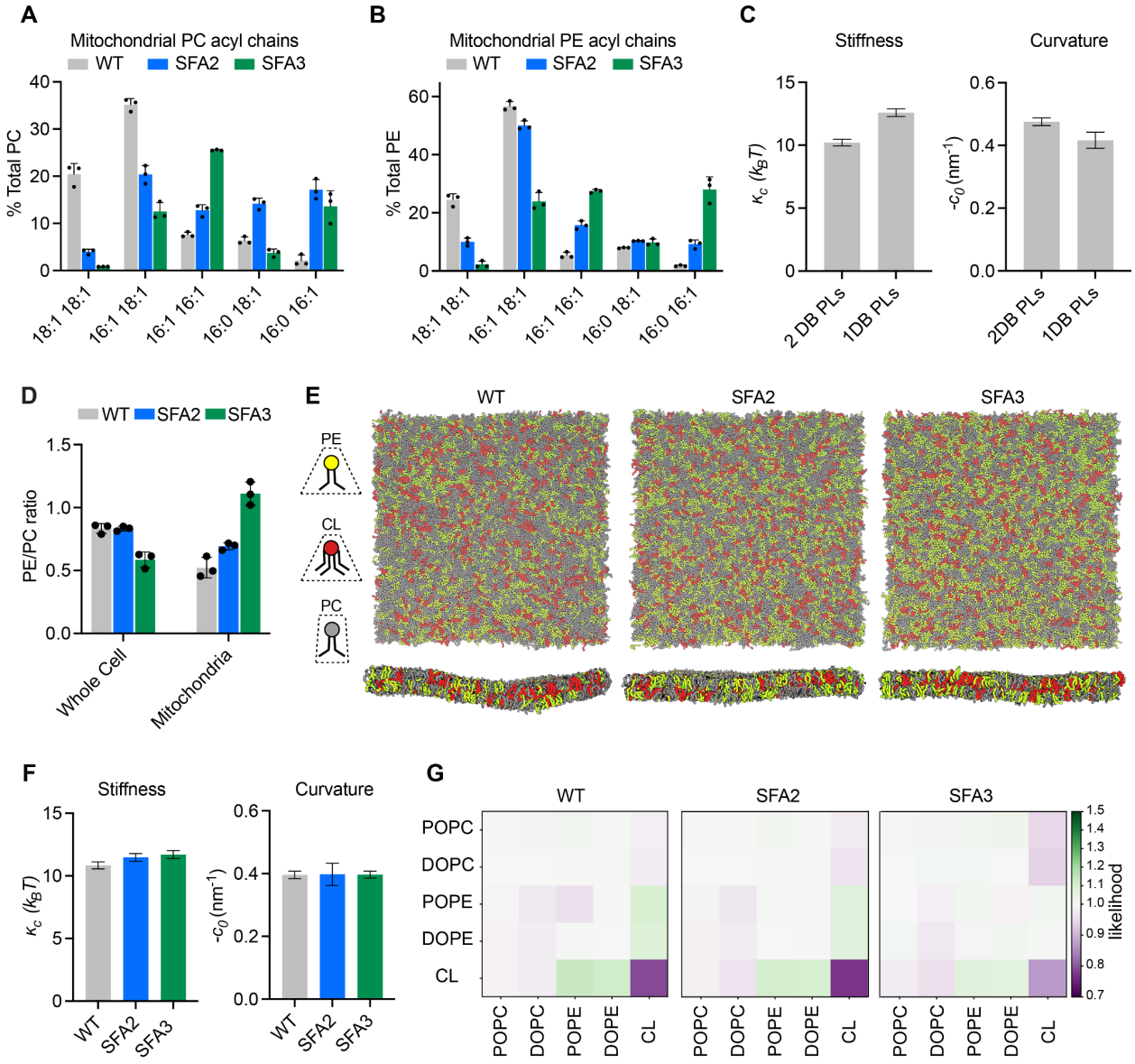

Figure 3: Modeling of lipid-driven mechanical changes in the IMM and their homeostatic responses.

(A) Lipidomic profile of isolated mitochondria showing a transition from di-unsaturated to monounsaturated PC, n=3. Error bars represent SD.

(B) Mitochondrial PE shows a similar transition from di-unsaturated species to monounsaturated species, n=3. Error bars represent SD.

(C) Changes to membrane mechanical properties predicted by Martini 2 CG-MD simulations of mitochondrial-like lipid mixtures that shift from di-unsaturated (2 double bonds, DB) to mono-unsaturated (1 DB) PLs. Stiffness (bending modulus) increases while negative spontaneous curvature, derived from the first moment of the lateral pressure profile and bending modulus, decreases. Compositions of these 'ideal' systems are shown in Figure S4A.

(D) Increasing lipid saturation reduces the PE/PC ratio in whole cells, but increases it in isolated mitochondria, suggesting a curvature based adaptation to increasing saturation.

(E) Top-down and side-on snapshots of CG-MD bilayers showing headgroup adaptation to increasing saturation in SFA strains.
(F) Simulations of the lipid systems derived from SFA mitochondria that incorporate homeostatic head-group changes. In contrast to the systems in (C), the complex systems show only small changes to membrane mechanical properties, suggesting that headgroup adaptations may offset the changes to mechanical properties associated with increased saturation.
(G) Likelihood relative to random that we observe lipids (x-axis) around a given lipid type (y-axis) in a 1.5 nm neighborhood. PO/DOPE molecules are enriched around CL, indicating the potential association between conically shaped lipids in the IMM.

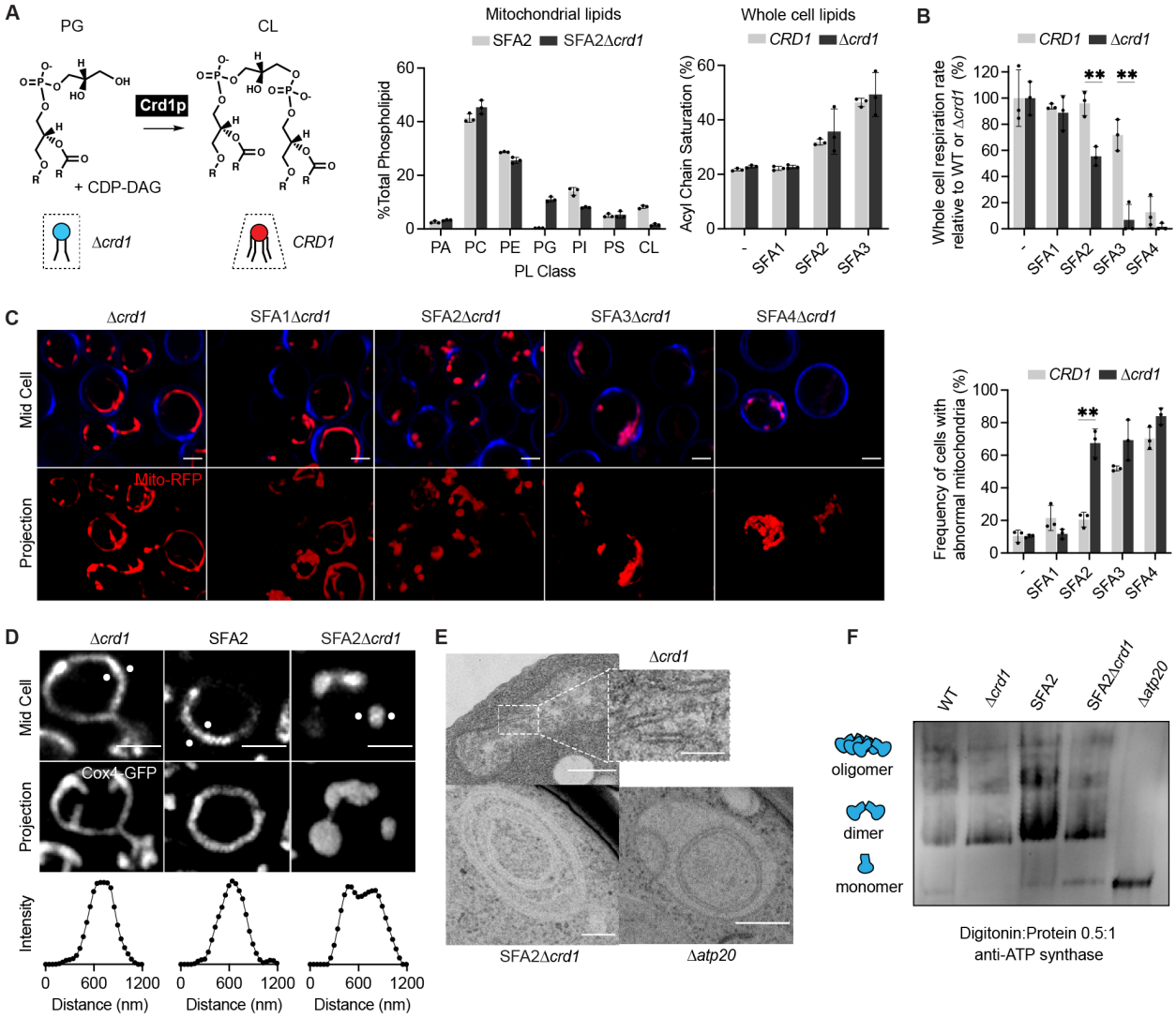

Figure 4: Epistasis between PL saturation and CL synthesis in shaping mitochondrial morphology.

(A) Loss of Crd1p decreases mitochondrial CL content, but otherwise does not affect the lipidome of SFA strains. (Left) Reaction schematic depicting cylindrical PG and CDP-DAG converted into conical CL by Crd1p. (Right) Head-group stoichiometry of lipidomes from isolated mitochondria from SFA2 and SFA2Δ*crd1* cells and acyl chain saturation (% of acyl chains with a double bond) for *CRD1* and Δ*crd1* cells across the SFA series. Error bars indicate SD from n=3 biological replicates.

(B) Loss of CL causes a loss of respiration in SFA2 cells. Whole cell respiration rates are shown for SFA strains, comparing *CRD1* with Δ*crd1* cells. Respirometry was conducted in biological triplicates (n=3) by Clark electrode. Error bars indicate SD. **p<0.005 unpaired two-tailed t-test between SFA2 and SFA3 strains and their corresponding Δ*crd1* mutants.

(C) The morphological breakpoint shifts to SFA2 upon loss of CL. (Left) Representative Airyscan confocal micrographs of yeast expressing matrix-localized RFP (mts-RFP). Cells were stained cell wall-binding calcofluor white (blue) for clarity. Scale bars, 2 μm. (Right) Frequency of mitochondrial abnormality, N>50 cells were counted in n=3 independent cultures for each

condition. Error bars indicate SD. **p=0.0011 unpaired two-tailed t-test between *CRD1* and Δ*crd1* in the SFA2 background.
(D) SFA2Δ*crd1* cells show hollow mitochondria, imaged with Cox4-GFP. Scale bars, 2 μm. Line profile analysis (below) depicts fluorescent intensity across the indicated mitochondria.
(E) Thin section TEM micrographs of Δ*crd1* show IMM with cristae invaginations (see inset, scale bars 100 nm), while SFA2Δ*crd1* cells show an onion-like IMM similar to what has been observed in Δ*atp20*. Scale bars, 400 nm.
(F) SFA2Δ*crd1* retains ATP synthase dimerization. Shown are BN-PAGE western blots run from digitonin-solubilized isolated mitochondria of SFA strains and WT with and without CL. Δ*atp20* is the monomeric ATP synthase control.

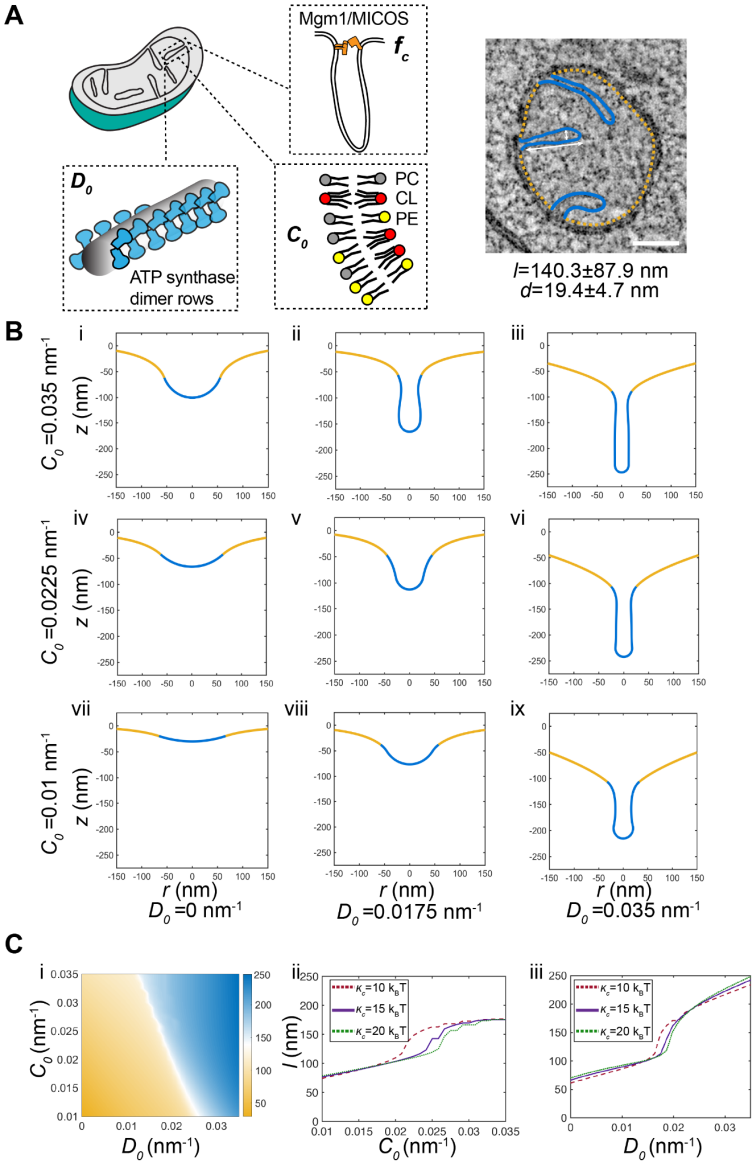

Figure 5: Continuum modeling of CM tubule formation reveals a snap-through instability mediated by both lipid and ATP synthase generated curvatures.

(A) Schematic depiction of yeast CM tubules containing a modeled neck force (f_c) induced by Mgm1p and MICOS complexes, a deviatoric curvature imposed by ATP synthase at tubule ridges (D_0), and a spontaneous curvature along the entire membrane imposed by asymmetric distribution of CL across the IMM (C_0). (Right) TEM image showing typical yeast CM tubules in a single mitochondrion. Scale bars, 100 nm. The average tubule length (140.3±87.9nm) and diameter (19.4±4.7nm) of 15 cristae tubules were analyzed from tomograms of n=3 SFA2 mitochondria.

(B) Changes in deviatory and spontaneous curvatures modulates tubule morphology. Panels i-ix show shapes of the membranes from simulations of the continuum model. For these simulations, the bending modulus of the membrane was maintained at 15 k_BT and the tension was set at 0.01 pN/nm. The total membrane area was set to 5.65 x 10^5 nm^2 and the coated area was 1.413 x 10^4 nm^2. The values of C_0 and D_0 were varied as shown and f_c was set to 8 pN/nm at the base of the coat.

(C) CM tubule formation shows a snap-through behavior. (i) Length of the tube as a function of C_0 and D_0 for the same values of bending modulus, tension, and areas as shown in (B). The white region shows the transition from the short to the long tube. The color bar shows the length of the tube in nm. Line graphs in (ii) show the length of the tube as a function of C_0 for D_0 fixed at 0.0175 nm^{-1} and and line graphs in (iii) show the length of the tube as a function of D_0 for C_0 fixed at 0.0225 nm^{-1} for three different values of κ. In both these graphs, the abrupt change in length is indicative of a snapthrough instability.

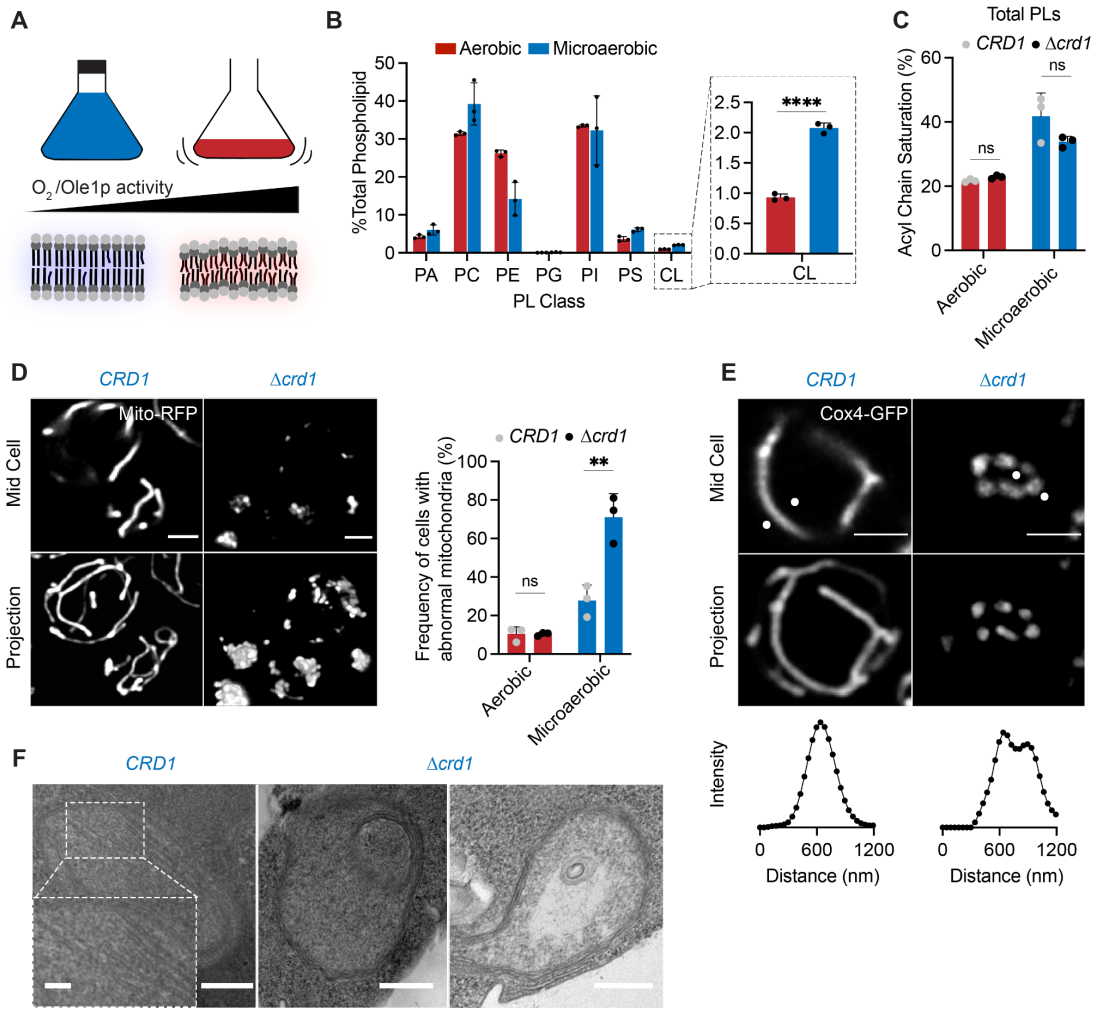

Figure 6: Cardiolipin synthesis is essential for mitochondria in yeast growth conditions characterized by low oxygenation.

(A) Schematic representation of different oxygen concentrations in different yeast growth environments. Microaerobic conditions cause increased saturation of membranes due to lower desaturate activity of Ole1p, an oxygen dependent enzyme.

(B) WT cells increase the abundance of CL under microaerobic conditions. Shown are abundances of each PL class, n=3. Error bars indicate SD. ****p < 0.0001, unpaired two-tailed t-test compared against wild-type.

(C) Microaerobic growth conditions cause an increase in acyl chain saturation in the total PL pool, which is not affected by loss of CL in Δ*crd1* strains. Error bars indicate SD from n=3 biological replicates.

(D) Under microaerobic conditions, loss of CL (Δ*crd1*) causes loss of tubular mitochondrial structure. WT (*CRD1*) and Δ*crd1* cells were grown in microaerobic chambers for 48 hours prior to imaging, n=3. Scale bars, 2 μm. **p < 0.005, unpaired two-tailed t-test compared against WT.

(E) Microaerobic Δ*crd1* show hollow mitochondria, imaged with Cox4-GFP. Scale bars, 2 μm. Line profile analysis (below) depicts fluorescent intensity across the indicated mitochondria.

(F) Under microaerobic conditions, *CRD1* cells contain long, sheet-like cristae structures while Δ*crd1* cells lack cristae, and display both onion-like and flat abnormal IMM structures as visualized by thin-section TEM. Scale bars, 250 nm. Inset showing abundant cristae sheets in *CRD1* cells, scale bar, 125 nm.

References

1. Nunnari, J., and Suomalainen, A. (2012). Mitochondria: In Sickness and in Health. Cell *148*, 1145–1159. 10.1016/j.cell.2012.02.035.

2. Daems, W.T., and Wisse, E. (1966). Shape and attachment of the cristae mitochondriales in mouse hepatic cell mitochondria. J. Ultrastruct. Res. *16*, 123–140.

3. Perkins, G., Renken, C., Martone, M.E., Young, S.J., Ellisman, M., and Frey, T. (1997). Electron tomography of neuronal mitochondria: three-dimensional structure and organization of cristae and membrane contacts. J. Struct. Biol. *119*, 260–272.

4. Revel, J.P., Fawcett, D.W., and Philpott, C.W. (1963). OBSERVATIONS ON MITOCHONDRIAL STRUCTURE. Journal of Cell Biology *16*, 187–195. 10.1083/jcb.16.1.187.

5. Mannella, C.A. (2006). Structure and dynamics of the mitochondrial inner membrane cristae. Biochim. Biophys. Acta *1763*, 542–548.

6. Zick, M., Rabl, R., and Reichert, A.S. (2009). Cristae formation—linking ultrastructure and function of mitochondria. Biochimica et Biophysica Acta (BBA) - Molecular Cell Research *1793*, 5–19.

7. Mendelsohn, R., Garcia, G.C., Bartol, T.M., Lee, C.T., Khandelwal, P., Liu, E., Spencer, D.J., Husar, A., Bushong, E.A., Phan, S., et al. (2022). Morphological principles of neuronal mitochondria. Journal of Comparative Neurology *530*, 886–902. 10.1002/cne.25254.

8. Pánek, T., Eliáš, M., Vancová, M., Lukeš, J., and Hashimi, H. (2020). Returning to the Fold for Lessons in Mitochondrial Crista Diversity and Evolution. Current Biology *30*, R575–R588. 10.1016/j.cub.2020.02.053.

9. Davies, K.M., Strauss, M., Daum, B., Kief, J.H., Osiewacz, H.D., Rycovska, A., Zickermann, V., and Kühlbrandt, W. (2011). Macromolecular organization of ATP synthase and complex I in whole mitochondria. Proc. Natl. Acad. Sci. U. S. A. *108*, 14121–14126.

10. Rieger, B., Junge, W., and Busch, K.B. (2014). Lateral pH gradient between OXPHOS complex IV and F0F1 ATP-synthase in folded mitochondrial membranes. Nature Communications *5*. 10.1038/ncomms4103.

11. Cogliati, S., Enriquez, J.A., and Scorrano, L. (2016). Mitochondrial Cristae: Where Beauty Meets Functionality. Trends in Biochemical Sciences *41*, 261–273. 10.1016/j.tibs.2016.01.001.

12. Mannella, C.A., Marko, M., and Buttle, K. (1997). Reconsidering mitochondrial structure: new views of an old organelle. Trends in Biochemical Sciences *22*, 37–38. 10.1016/s0968-0004(96)30050-9.

13. Mannella, C.A. (2006). The relevance of mitochondrial membrane topology to mitochondrial function. Biochimica et Biophysica Acta (BBA) - Molecular Basis of Disease *1762*, 140–147. 10.1016/j.bbadis.2005.07.001.

14. Mannella, C.A., Marko, M., Penczek, P., Barnard, D., and Frank, J. (1994). The internal

compartmentation of rat-liver mitochondria: Tomographic study using the high-voltage transmission electron microscope. Microscopy Research and Technique *27*, 278–283. 10.1002/jemt.1070270403.

15. Frey, T.G., and Mannella, C.A. (2000). The internal structure of mitochondria. Trends in Biochemical Sciences *25*, 319–324. 10.1016/s0968-0004(00)01609-1.

16. Dudkina, N.V., Heinemeyer, J., Keegstra, W., Boekema, E.J., and Braun, H.-P. (2005). Structure of dimeric ATP synthase from mitochondria: an angular association of monomers induces the strong curvature of the inner membrane. FEBS Lett. *579*, 5769–5772.

17. Strauss, M., Hofhaus, G., Schröder, R.R., and Kühlbrandt, W. (2008). Dimer ribbons of ATP synthase shape the inner mitochondrial membrane. EMBO J. *27*, 1154–1160.

18. Blum, T.B., Hahn, A., Meier, T., Davies, K.M., and Kühlbrandt, W. (2019). Dimers of mitochondrial ATP synthase induce membrane curvature and self-assemble into rows. Proc. Natl. Acad. Sci. U. S. A. *116*, 4250–4255.

19. Paumard, P., Vaillier, J., Coulary, B., Schaeffer, J., Soubannier, V., Mueller, D.M., Brèthes, D., di Rago, J.-P., and Velours, J. (2002). The ATP synthase is involved in generating mitochondrial cristae morphology. EMBO J. *21*, 221–230.

20. Arnold, I., Pfeiffer, K., Neupert, W., Stuart, R.A., and Schägger, H. (1998). Yeast mitochondrial F1F0-ATP synthase exists as a dimer: identification of three dimer-specific subunits. EMBO J. *17*, 7170–7178.

21. Arselin, G., Vaillier, J., Salin, B., Schaeffer, J., Giraud, M.-F., Dautant, A., Brèthes, D., and Velours, J. (2004). The modulation in subunits e and g amounts of yeast ATP synthase modifies mitochondrial cristae morphology. J. Biol. Chem. *279*, 40392–40399.

22. Rabl, R., Soubannier, V., Scholz, R., Vogel, F., Mendl, N., Vasiljev-Neumeyer, A., Körner, C., Jagasia, R., Keil, T., Baumeister, W., et al. (2009). Formation of cristae and crista junctions in mitochondria depends on antagonism between Fcj1 and Su e/g. J. Cell Biol. *185*, 1047–1063.

23. Anselmi, C., Davies, K.M., and Faraldo-Gómez, J.D. (2018). Mitochondrial ATP synthase dimers spontaneously associate due to a long-range membrane-induced force. J. Gen. Physiol., jgp.201812033.

24. Harner, M., Körner, C., Walther, D., Mokranjac, D., Kaesmacher, J., Welsch, U., Griffith, J., Mann, M., Reggiori, F., and Neupert, W. (2011). The mitochondrial contact site complex, a determinant of mitochondrial architecture. EMBO J. *30*, 4356–4370.

25. Hoppins, S., Collins, S.R., Cassidy-Stone, A., Hummel, E., Devay, R.M., Lackner, L.L., Westermann, B., Schuldiner, M., Weissman, J.S., and Nunnari, J. (2011). A mitochondrial-focused genetic interaction map reveals a scaffold-like complex required for inner membrane organization in mitochondria. J. Cell Biol. *195*, 323–340.

26. Glytsou, C., Calvo, E., Cogliati, S., Mehrotra, A., Anastasia, I., Rigoni, G., Raimondi, A., Shintani, N., Loureiro, M., Vazquez, J., et al. (2016). Optic Atrophy 1 Is Epistatic to the Core MICOS Component MIC60 in Mitochondrial Cristae Shape Control. Cell Rep. *17*, 3024–3034.

27. Frezza, C., Cipolat, S., Martins de Brito, O., Micaroni, M., Beznoussenko, G.V., Rudka, T., Bartoli, D., Polishuck, R.S., Danial, N.N., De Strooper, B., et al. (2006). OPA1 controls apoptotic cristae remodeling independently from mitochondrial fusion. Cell *126*, 177–189.

28. Patten, D.A., Wong, J., Khacho, M., Soubannier, V., Mailloux, R.J., Pilon-Larose, K., MacLaurin, J.G., Park, D.S., McBride, H.M., Trinkle-Mulcahy, L., et al. (2014). OPA1-dependent cristae modulation is essential for cellular adaptation to metabolic demand. EMBO J. *33*, 2676–2691.

29. Hu, C., Shu, L., Huang, X., Yu, J., Li, L., Gong, L., Yang, M., Wu, Z., Gao, Z., Zhao, Y., et al. (2020). OPA1 and MICOS Regulate mitochondrial crista dynamics and formation. Cell Death Dis. *11*, 940.

30. Harner, M.E., Unger, A.-K., Geerts, W.J., Mari, M., Izawa, T., Stenger, M., Geimer, S., Reggiori, F., Westermann, B., and Neupert, W. (2016). An evidence based hypothesis on the existence of two pathways of mitochondrial crista formation. Elife *5*. 10.7554/eLife.18853.

31. Sesaki, H., Southard, S.M., Yaffe, M.P., and Jensen, R.E. (2003). Mgm1p, a dynamin-related GTPase, is essential for fusion of the mitochondrial outer membrane. Mol. Biol. Cell *14*, 2342–2356.

32. Zinser, E., Sperka-Gottlieb, C.D., Fasch, E.V., Kohlwein, S.D., Paltauf, F., and Daum, G. (1991). Phospholipid synthesis and lipid composition of subcellular membranes in the unicellular eukaryote Saccharomyces cerevisiae. Journal of Bacteriology *173*, 2026–2034. 10.1128/jb.173.6.2026-2034.1991.

33. Mejia, E.M., and Hatch, G.M. (2016). Mitochondrial phospholipids: role in mitochondrial function. Journal of Bioenergetics and Biomembranes *48*, 99–112. 10.1007/s10863-015-9601-4.

34. Horvath, S.E., and Daum, G. (2013). Lipids of mitochondria. Progress in Lipid Research *52*, 590–614. 10.1016/j.plipres.2013.07.002.

35. LeCocq, J., and Ballou, C.E. (1964). On the Structure of Cardiolipin*. Biochemistry *3*, 976–980. 10.1021/bi00895a023.

36. Beltrán-Heredia, E., Tsai, F.-C., Salinas-Almaguer, S., Cao, F.J., Bassereau, P., and Monroy, F. (2019). Membrane curvature induces cardiolipin sorting. Communications Biology *2*. 10.1038/s42003-019-0471-x.

37. Olofsson, G., and Sparr, E. (2013). Ionization constants pKa of cardiolipin. PLoS One *8*, e73040.

38. Kates, M., Syz, J.Y., Gosser, D., and Haines, T.H. (1993). pH-dissociation characteristics of cardiolipin and its 2'-deoxy analogue. Lipids *28*, 877–882.

39. Sturm, M., Gutowski, O., and Brezesinski, G. (2022). The effect of pH on the structure and lateral organization of cardiolipin in Langmuir monolayers. Chemphyschem *23*, e202200218.

40. Khalifat, N., Puff, N., Bonneau, S., Fournier, J.-B., and Angelova, M.I. (2008). Membrane

Deformation under Local pH Gradient: Mimicking Mitochondrial Cristae Dynamics. Biophysical Journal *95*, 4924–4933. 10.1529/biophysj.108.136077.

41. Khalifat, N., Fournier, J.-B., Angelova, M.I., and Puff, N. (2011). Lipid packing variations induced by pH in cardiolipin-containing bilayers: The driving force for the cristae-like shape instability. Biochimica et Biophysica Acta (BBA) - Biomembranes *1808*, 2724–2733. 10.1016/j.bbamem.2011.07.013.

42. Ikon, N., and Ryan, R.O. (2017). Cardiolipin and mitochondrial cristae organization. Biochimica et Biophysica Acta (BBA) - Biomembranes *1859*, 1156–1163. 10.1016/j.bbamem.2017.03.013.

43. Chen, Y.-F., Tsang, K.-Y., Chang, W.-F., and Fan, Z.-A. (2015). Differential dependencies on [Ca^2] and temperature of the monolayer spontaneous curvatures of DOPE, DOPA and cardiolipin: effects of modulating the strength of the inter-headgroup repulsion. Soft Matter *11*, 4041–4053. 10.1039/c5sm00577a.

44. Dahlberg, M., and Maliniak, A. (2010). Mechanical Properties of Coarse-Grained Bilayers Formed by Cardiolipin and Zwitterionic Lipids. J. Chem. Theory Comput. *6*, 1638–1649.

45. Konar, S., Arif, H., and Allolio, C. (2023). Mitochondrial Membranes: Model Lipid Compositions, Material Properties and the Changing Curvature of Cardiolipin. bioRxiv, 2023.02.06.527315. 10.1101/2023.02.06.527315.

46. Adès, L.C., Gedeon, A.K., Wilson, M.J., Latham, M., Partington, M.W., Mulley, J.C., Nelson, J., Lui, K., and Sillence, D.O. (1993). Barth syndrome: Clinical features and confirmation of gene localisation to distal Xq28. American Journal of Medical Genetics *45*, 327–334. 10.1002/ajmg.1320450309.

47. Bione, S., D'Adamo, P., Maestrini, E., Gedeon, A.K., Bolhuis, P.A., and Toniolo, D. (1996). A novel X-linked gene, G4.5. is responsible for Barth syndrome. Nature Genetics *12*, 385–389. 10.1038/ng0496-385.

48. Acehan, D., Xu, Y., Stokes, D.L., and Schlame, M. (2007). Comparison of lymphoblast mitochondria from normal subjects and patients with Barth syndrome using electron microscopic tomography. Laboratory Investigation *87*, 40–48. 10.1038/labinvest.3700480.

49. Claypool, S.M., and Koehler, C.M. (2012). The complexity of cardiolipin in health and disease. Trends in Biochemical Sciences *37*, 32–41. 10.1016/j.tibs.2011.09.003.

50. Ren, M., Phoon, C.K.L., and Schlame, M. (2014). Metabolism and function of mitochondrial cardiolipin. Progress in Lipid Research *55*, 1–16. 10.1016/j.plipres.2014.04.001.

51. Paradies, G., Paradies, V., Ruggiero, F.M., and Petrosillo, G. (2019). Role of Cardiolipin in Mitochondrial Function and Dynamics in Health and Disease: Molecular and Pharmacological Aspects. Cells *8*, 728. 10.3390/cells8070728.

52. Baile, M.G., Sathappa, M., Lu, Y.-W., Pryce, E., Whited, K., Michael McCaffery, J., Han, X., Alder, N.N., and Claypool, S.M. (2014). Unremodeled and Remodeled Cardiolipin Are Functionally Indistinguishable in Yeast. Journal of Biological Chemistry *289*, 1768–1778. 10.1074/jbc.m113.525733.

53. Jiang, F., Rizavi, H.S., and Greenberg, M.L. (1997). Cardiolipin is not essential for the growth of Saccharomyces cerevisiae on fermentable or non-fermentable carbon sources. Mol. Microbiol. *26*, 481–491.

54. Xu, Y., Erdjument-Bromage, H., Phoon, C.K.L., Neubert, T.A., Ren, M., and Schlame, M. (2021). Cardiolipin remodeling enables protein crowding in the inner mitochondrial membrane. EMBO J. *40*, e108428.

55. Zhang, M., Mileykovskaya, E., and Dowhan, W. (2005). Cardiolipin Is Essential for Organization of Complexes III and IV into a Supercomplex in Intact Yeast Mitochondria. Journal of Biological Chemistry *280*, 29403–29408. 10.1074/jbc.m504955200.

56. Harayama, T., and Riezman, H. (2019). Author Correction: Understanding the diversity of membrane lipid composition. Nature Reviews Molecular Cell Biology *20*, 715–715. 10.1038/s41580-019-0171-x.

57. Filippov, A., Orädd, G., and Lindblom, G. (2003). The Effect of Cholesterol on the Lateral Diffusion of Phospholipids in Oriented Bilayers. Biophysical Journal *84*, 3079–3086. 10.1016/s0006-3495(03)70033-2.

58. Vance, J.E. (2015). Phospholipid Synthesis and Transport in Mammalian Cells. Traffic *16*, 1–18. 10.1111/tra.12230.

59. Bard, M. (1972). Biochemical and Genetic Aspects of Nystatin Resistance in *Saccharomyces cerevisiae*. Journal of Bacteriology *111*, 649–657. 10.1128/jb.111.3.649-657.1972.

60. Stukey, J.E., McDonough, V.M., and Martin, C.E. (1989). Isolation and characterization of OLE1, a gene affecting fatty acid desaturation from Saccharomyces cerevisiae. Journal of Biological Chemistry *264*, 16537–16544. 10.1016/s0021-9258(19)84740-3.

61. McConnell, S.J., Stewart, L.C., Talin, A., and Yaffe, M.P. (1990). Temperature-sensitive yeast mutants defective in mitochondrial inheritance. Journal of Cell Biology *111*, 967–976. 10.1083/jcb.111.3.967.

62. Stewart, L.C., and Yaffe, M.P. (1991). A role for unsaturated fatty acids in mitochondrial movement and inheritance. The Journal of Cell Biology *115*, 1249–1257. 10.1083/jcb.115.5.1249.

63. Penzo, D., Tagliapietra, C., Colonna, R., Petronilli, V., and Bernardi, P. (2002). Effects of fatty acids on mitochondria: implications for cell death. Biochimica et Biophysica Acta (BBA) - Bioenergetics *1555*, 160–165. 10.1016/s0005-2728(02)00272-4.

64. Sparagna, G.C., Hickson-Bick, D.L., Maximilian Buja, L., and McMillin, J.B. (2000). A metabolic role for mitochondria in palmitate-induced cardiac myocyte apoptosis. American Journal of Physiology-Heart and Circulatory Physiology *279*, H2124–H2132. 10.1152/ajpheart.2000.279.5.h2124.

65. Jheng, H.-F., Tsai, P.-J., Guo, S.-M., Kuo, L.-H., Chang, C.-S., Su, I.-J., Chang, C.-R., and Tsai, Y.-S. (2012). Mitochondrial Fission Contributes to Mitochondrial Dysfunction and Insulin Resistance in Skeletal Muscle. Molecular and Cellular Biology *32*, 309–319. 10.1128/mcb.05603-11.

66. Petersen, K.F., Dufour, S., Befroy, D., Garcia, R., and Shulman, G.I. (2004). Impaired Mitochondrial Activity in the Insulin-Resistant Offspring of Patients with Type 2 Diabetes. New England Journal of Medicine *350*, 664–671. 10.1056/nejmoa031314.

67. Lowell, B.B., and Shulman, G.I. (2005). Mitochondrial Dysfunction and Type 2 Diabetes. Science *307*, 384–387. 10.1126/science.1104343.

68. Budin, I., de Rond, T., Chen, Y., Chan, L.J.G., Petzold, C.J., and Keasling, J.D. (2018). Viscous control of cellular respiration by membrane lipid composition. Science *362*, 1186–1189. 10.1126/science.aat7925.

69. Raote, I., Chabanon, M., Walani, N., Arroyo, M., Garcia-Parajo, M.F., Malhotra, V., and Campelo, F. (2020). A physical mechanism of TANGO1-mediated bulky cargo export. Elife *9*. 10.7554/eLife.59426.

70. Alimohamadi, H., Bell, M.K., Halpain, S., and Rangamani, P. (2021). Mechanical Principles Governing the Shapes of Dendritic Spines. Front. Physiol. *12*, 657074.

71. Alimohamadi, H., Smith, A.S., Nowak, R.B., Fowler, V.M., and Rangamani, P. (2020). Non-uniform distribution of myosin-mediated forces governs red blood cell membrane curvature through tension modulation. PLoS Comput. Biol. *16*, e1007890.

72. Kozlov, M.M., Campelo, F., Liska, N., Chernomordik, L.V., Marrink, S.J., and McMahon, H.T. (2014). Mechanisms shaping cell membranes. Curr. Opin. Cell Biol. *29*, 53–60.

73. Yuan, F., Alimohamadi, H., Bakka, B., Trementozzi, A.N., Day, K.J., Fawzi, N.L., Rangamani, P., and Stachowiak, J.C. (2021). Membrane bending by protein phase separation. Proc. Natl. Acad. Sci. U. S. A. *118*. 10.1073/pnas.2017435118.

74. Fowler, P.W., Hélie, J., Duncan, A., Chavent, M., Koldsø, H., and Sansom, M.S.P. (2016). Membrane stiffness is modified by integral membrane proteins. Soft Matter *12*, 7792–7803.

75. Lindahl, E., and Sansom, M.S.P. (2008). Membrane proteins: molecular dynamics simulations. Curr. Opin. Struct. Biol. *18*, 425–431.

76. Venable, R.M., Brown, F.L.H., and Pastor, R.W. (2015). Mechanical properties of lipid bilayers from molecular dynamics simulation. Chem. Phys. Lipids *192*, 60–74.

77. Chabanon, M., Stachowiak, J.C., and Rangamani, P. (2017). Systems biology of cellular membranes: a convergence with biophysics. Wiley Interdiscip. Rev. Syst. Biol. Med. *9*, e1386.

78. Rangamani, P. (2022). The many faces of membrane tension: Challenges across systems and scales. Biochim. Biophys. Acta Biomembr. *1864*, 183897.

79. Steigmann, D.J. (2017). The Role of Mechanics in the Study of Lipid Bilayers (Springer).

80. Helfrich, W. (1973). Elastic Properties of Lipid Bilayers: Theory and Possible Experiments. Zeitschrift für Naturforschung C *28*, 693–703. 10.1515/znc-1973-11-1209.

81. Canham, P.B. (1970). The minimum energy of bending as a possible explanation of the biconcave shape of the human red blood cell. J. Theor. Biol. *26*, 61–81.

82. Evans, E.A. (1973). A new material concept for the red cell membrane. Biophys. J. *13*, 926–940.

83. Manni, M.M., Tiberti, M.L., Pagnotta, S., Barelli, H., Gautier, R., and Antonny, B. (2018). Acyl chain asymmetry and polyunsaturation of brain phospholipids facilitate membrane vesiculation without leakage. Elife *7*. 10.7554/eLife.34394.

84. Rawicz, W., Olbrich, K.C., McIntosh, T., Needham, D., and Evans, E. (2000). Effect of Chain Length and Unsaturation on Elasticity of Lipid Bilayers. Biophysical Journal *79*, 328–339. 10.1016/s0006-3495(00)76295-3.

85. Schiaffarino, O., Valdivieso González, D., García-Pérez, I.M., Peñalva, D.A., Almendro-Vedia, V.G., Natale, P., and López-Montero, I. (2022). Mitochondrial membrane models built from native lipid extracts: Interfacial and transport properties. Front Mol Biosci *9*, 910936.

86. Dymond, M.K. (2021). Lipid monolayer spontaneous curvatures: A collection of published values. Chem. Phys. Lipids *239*, 105117.

87. Szule, J.A., Fuller, N.L., and Rand, R.P. (2002). The effects of acyl chain length and saturation of diacylglycerols and phosphatidylcholines on membrane monolayer curvature. Biophys. J. *83*, 977–984.

88. Dawaliby, R., Trubbia, C., Delporte, C., Noyon, C., Ruysschaert, J.-M., Van Antwerpen, P., and Govaerts, C. (2016). Phosphatidylethanolamine Is a Key Regulator of Membrane Fluidity in Eukaryotic Cells. Journal of Biological Chemistry *291*, 3658–3667. 10.1074/jbc.m115.706523.

89. Janssen, M.J.F.W., Janssen, M.J.F., Koorengevel, M.C., de Kruijff, B., and de Kroon, A.I.P.M. (2000). The phosphatidylcholine to phosphatidylethanolamine ratio ofSaccharomyces cerevisiae varies with the growth phase. Yeast *16*, 641–650. 10.1002/(sici)1097-0061(200005)16:7<641::aid-yea578>3.0.co;2-u.

90. Al-Fageeh, M.B., and Mark Smales, C. (2006). Control and regulation of the cellular responses to cold shock: the responses in yeast and mammalian systems. Biochemical Journal *397*, 247–259. 10.1042/bj20060166.

91. Lee, C.T., Laughlin, J.G., Angliviel de La Beaumelle, N., Amaro, R.E., McCammon, J.A., Ramamoorthi, R., Holst, M., and Rangamani, P. (2020). 3D mesh processing using GAMer 2 to enable reaction-diffusion simulations in realistic cellular geometries. PLoS Comput. Biol. *16*, e1007756.

92. Lee, C.T., Laughlin, J.G., Moody, J.B., Amaro, R.E., McCammon, J.A., Holst, M.J., and Rangamani, P. (2020). An Open-Source Mesh Generation Platform for Biophysical Modeling Using Realistic Cellular Geometries. Biophys. J. *118*, 1003–1008.

93. Rangamani, P., Lipshtat, A., Azeloglu, E.U., Calizo, R.C., Hu, M., Ghassemi, S., Hone, J., Scarlata, S., Neves, S.R., and Iyengar, R. (2013). Decoding information in cell shape. Cell *154*, 1356–1369.

94. Calizo, R.C., Bell, M.K., Ron, A., Hu, M., Bhattacharya, S., Wong, N.J., Janssen, W.G.M., Perumal, G., Pederson, P., Scarlata, S., et al. (2020). Cell shape regulates subcellular

organelle location to control early Ca2+ signal dynamics in vascular smooth muscle cells. Sci. Rep. *10*, 17866.

95. Cugno, A., Bartol, T.M., Sejnowski, T.J., Iyengar, R., and Rangamani, P. (2019). Geometric principles of second messenger dynamics in dendritic spines. Sci. Rep., 444489. 10.1038/s41598-019-48028-0.

96. Bell, M.K., Holst, M.V., Lee, C.T., and Rangamani, P. (2022). Dendritic spine morphology regulates calcium-dependent synaptic weight change. bioRxiv, 2021.05.06.442994. 10.1101/2021.05.06.442994.

97. Garcia, G.C., Bartol, T.M., Phan, S., Bushong, E.A., Perkins, G., Sejnowski, T.J., Ellisman, M.H., and Skupin, A. (2019). Mitochondrial morphology provides a mechanism for energy buffering at synapses. Sci. Rep. *9*, 18306.

98. Husar, A., Ordyan, M., Garcia, G.C., Yancey, J.G., Saglam, A.S., Faeder, J.R., Bartol, T.M., and Sejnowski, T.J. (2022). MCell4 with BioNetGen: A Monte Carlo Simulator of Rule-Based Reaction-Diffusion Systems with Python Interface. bioRxiv, 2022.05.17.492333. 10.1101/2022.05.17.492333.

99. Marrink, S.J., and Tieleman, D.P. (2013). Perspective on the Martini model. Chem. Soc. Rev. *42*, 6801–6822.

100. Marrink, S.J., Corradi, V., Souza, P.C.T., Ingólfsson, H.I., Tieleman, D.P., and Sansom, M.S.P. (2019). Computational Modeling of Realistic Cell Membranes. Chem. Rev. *119*, 6184–6226.

101. Callan-Jones, A., Sorre, B., and Bassereau, P. (2011). Curvature-driven lipid sorting in biomembranes. Cold Spring Harb. Perspect. Biol. *3*. 10.1101/cshperspect.a004648.

102. Gallet, P.F., Petit, J.M., Maftah, A., Zachowski, A., and Julien, R. (1997). Asymmetrical distribution of cardiolipin in yeast inner mitochondrial membrane triggered by carbon catabolite repression. Biochem. J *324 (Pt 2)*, 627–634.

103. Mahapatra, A. (2022). Formation of protein-mediated tubes is governed by a snapthrough transition. bioRxiv, 2022.06.07.494774. 10.1101/2022.06.07.494774.

104. Hassinger, J.E., Oster, G., Drubin, D.G., and Rangamani, P. (2017). Design principles for robust vesiculation in clathrin-mediated endocytosis. Proc. Natl. Acad. Sci. U. S. A. *114*, E1118–E1127.

105. Alimohamadi, H., Vasan, R., Hassinger, J.E., Stachowiak, J.C., and Rangamani, P. (2018). The role of traction in membrane curvature generation. Mol. Biol. Cell *114*, 2024–2035.

106. Chabanon, M., and Rangamani, P. (2018). Gaussian curvature directs the distribution of spontaneous curvature on bilayer membrane necks. Soft Matter *14*, 2281–2294.

107. Powers, T.R., Huber, G., and Goldstein, R.E. (2002). Fluid-membrane tethers: minimal surfaces and elastic boundary layers. Phys. Rev. E Stat. Nonlin. Soft Matter Phys. *65*, 041901.

108. Walani, N., Torres, J., and Agrawal, A. (2015). Endocytic proteins drive vesicle growth via instability in high membrane tension environment. Proceedings of the National Academy of

Sciences *112*, 201418491.

109. Irajizad, E., Ramachandran, R., and Agrawal, A. (2018). Geometric instability catalyzes mitochondrial fission. Mol. Biol. Cell, mbcE18010018.

110. Schlame, M., Brody, S., and Hostetler, K.Y. (1993). Mitochondrial cardiolipin in diverse eukaryotes. Comparison of biosynthetic reactions and molecular acyl species. European Journal of Biochemistry *212*, 727–733. 10.1111/j.1432-1033.1993.tb17711.x.

111. Paradies, G., Paradies, V., De Benedictis, V., Ruggiero, F.M., and Petrosillo, G. (2014). Functional role of cardiolipin in mitochondrial bioenergetics. Biochimica et Biophysica Acta (BBA) - Bioenergetics *1837*, 408–417. 10.1016/j.bbabio.2013.10.006.

112. McKeon, T.A., and Stumpf, P.K. (1982). Purification and characterization of the stearoyl-acyl carrier protein desaturase and the acyl-acyl carrier protein thioesterase from maturing seeds of safflower. Journal of Biological Chemistry *257*, 12141–12147. 10.1016/s0021-9258(18)33690-1.

113. Vasconcelles, M.J., Jiang, Y., McDaid, K., Gilooly, L., Wretzel, S., Porter, D.L., Martin, C.E., and Goldberg, M.A. (2001). Identification and Characterization of a Low Oxygen Response Element Involved in the Hypoxic Induction of a Family ofSaccharomyces cerevisiae Genes. Journal of Biological Chemistry *276*, 14374–14384. 10.1074/jbc.m009546200.

114. Kwast, K.E., Burke, P.V., Staahl, B.T., and Poyton, R.O. (1999). Oxygen sensing in yeast: Evidence for the involvement of the respiratory chain in regulating the transcription of a subset of hypoxic genes. Proceedings of the National Academy of Sciences *96*, 5446–5451. 10.1073/pnas.96.10.5446.

115. Petit, J.M., Huet, O., Gallet, P.F., Maftah, A., Ratinaud, M.H., and Julien, R. (1994). Direct analysis and significance of cardiolipin transverse distribution in mitochondrial inner membranes. Eur. J. Biochem. *220*, 871–879.

116. Boyd, K.J., Alder, N.N., and May, E.R. (2017). Buckling Under Pressure: Curvature-Based Lipid Segregation and Stability Modulation in Cardiolipin-Containing Bilayers. Langmuir *33*, 6937–6946.

117. Spinelli, J.B., and Haigis, M.C. (2018). The multifaceted contributions of mitochondria to cellular metabolism. Nat. Cell Biol. *20*, 745–754.

118. Yadav, P.K., and Rajasekharan, R. (2016). Misregulation of a DDHD Domain-containing Lipase Causes Mitochondrial Dysfunction in Yeast. J. Biol. Chem. *291*, 18562–18581.

119. Kasahara, T., Kubota-Sakashita, M., Nagatsuka, Y., Hirabayashi, Y., Hanasaka, T., Tohyama, K., and Kato, T. (2020). Cardiolipin is essential for early embryonic viability and mitochondrial integrity of neurons in mammals. FASEB J. *34*, 1465–1480.

120. Choi, S.-Y., Gonzalvez, F., Jenkins, G.M., Slomianny, C., Chretien, D., Arnoult, D., Petit, P.X., and Frohman, M.A. (2007). Cardiolipin deficiency releases cytochrome c from the inner mitochondrial membrane and accelerates stimuli-elicited apoptosis. Cell Death Differ. *14*, 597–606.

121. Carvalho, M., Sampaio, J.L., Palm, W., Brankatschk, M., Eaton, S., and Shevchenko, A.

(2012). Effects of diet and development on the Drosophila lipidome. Mol. Syst. Biol. *8*, 600.

122. van der Veen, J.N., Kennelly, J.P., Wan, S., Vance, J.E., Vance, D.E., and Jacobs, R.L. (2017). The critical role of phosphatidylcholine and phosphatidylethanolamine metabolism in health and disease. Biochim. Biophys. Acta Biomembr. *1859*, 1558–1572.

123. Montoya, M.T., Porres, A., Serrano, S., Fruchart, J.C., Mata, P., Gerique, J.A.G., and Castro, G.R. (2002). Fatty acid saturation of the diet and plasma lipid concentrations, lipoprotein particle concentrations, and cholesterol efflux capacity. Am. J. Clin. Nutr. *75*, 484–491.

124. Ou-Yang, Z.-C., Liu, J.-X., Xie, Y.-Z., and Yu-Zhang, X. (1999). Geometric Methods in the Elastic Theory of Membranes in Liquid Crystal Phases (World Scientific).

125. Vasan, R., Rudraraju, S., Akamatsu, M., Garikipati, K., and Rangamani, P. (2020). A mechanical model reveals that non-axisymmetric buckling lowers the energy barrier associated with membrane neck constriction. Soft Matter *16*, 784–797.

126. Hu, J., Shibata, Y., Voss, C., Shemesh, T., Li, Z., Coughlin, M., Kozlov, M.M., Rapoport, T.A., and Prinz, W.A. (2008). Membrane proteins of the endoplasmic reticulum induce high-curvature tubules. Science *319*, 1247–1250.

127. Ladinsky, M.S., Mastronarde, D.N., McIntosh, J.R., Howell, K.E., and Staehelin, L.A. (1999). Golgi structure in three dimensions: functional insights from the normal rat kidney cell. J. Cell Biol. *144*, 1135–1149.

128. Shibata, Y., Shemesh, T., Prinz, W.A., Palazzo, A.F., Kozlov, M.M., and Rapoport, T.A. (2010). Mechanisms Determining the Morphology of the Peripheral ER. Cell *143*, 774–788. 10.1016/j.cell.2010.11.007.

129. Derganc, J. (2007). Curvature-driven lateral segregation of membrane constituents in Golgi cisternae. Physical Biology *4*, 317–324. 10.1088/1478-3975/4/4/008.

130. Covino, R., Ballweg, S., Stordeur, C., Michaelis, J.B., Puth, K., Wernig, F., Bahrami, A., Ernst, A.M., Hummer, G., and Ernst, R. (2016). A Eukaryotic Sensor for Membrane Lipid Saturation. Mol. Cell *63*, 49–59.

131. Ballweg, S., Sezgin, E., Doktorova, M., Covino, R., Reinhard, J., Wunnicke, D., Hänelt, I., Levental, I., Hummer, G., and Ernst, R. (2020). Regulation of lipid saturation without sensing membrane fluidity. Nat. Commun. *11*, 756.

132. Chadda, R., Krishnamani, V., Mersch, K., Wong, J., Brimberry, M., Chadda, A., Kolmakova-Partensky, L., Friedman, L.J., Gelles, J., and Robertson, J.L. (2016). The dimerization equilibrium of a ClC Cl(-)/H(+) antiporter in lipid bilayers. Elife *5*. 10.7554/eLife.17438.

133. Chadda, R., Bernhardt, N., Kelley, E.G., Teixeira, S.C., Griffith, K., Gil-Ley, A., Öztürk, T.N., Hughes, L.E., Forsythe, A., Krishnamani, V., et al. (2021). Membrane transporter dimerization driven by differential lipid solvation energetics of dissociated and associated states. Elife *10*. 10.7554/eLife.63288.

134. Guo, H., Bueler, S.A., and Rubinstein, J.L. (2017). Atomic model for the dimeric FO region

of mitochondrial ATP synthase. Science *358*, 936–940.

135. Rowlett, V.W., Mallampalli, V.K.P.S., Karlstaedt, A., Dowhan, W., Taegtmeyer, H., Margolin, W., and Vitrac, H. (2017). Impact of Membrane Phospholipid Alterations in Escherichia coli on Cellular Function and Bacterial Stress Adaptation. J. Bacteriol. *199*. 10.1128/JB.00849-16.

136. Sohlenkamp, C., and Geiger, O. (2016). Bacterial membrane lipids: diversity in structures and pathways. FEMS Microbiol. Rev. *40*, 133–159.

137. Galber, C., Valente, G., von Stockum, S., and Giorgio, V. (2019). Purification of Functional F-ATP Synthase from Blue Native PAGE. Methods Mol. Biol. *1925*, 233–243.

138. Bisetto, E., Di Pancrazio, F., Simula, M.P., Mavelli, I., and Lippe, G. (2007). Mammalian ATPsynthase monomer versus dimer profiled by blue native PAGE and activity stain. Electrophoresis *28*, 3178–3185.

139. Huynen, M.A., Mühlmeister, M., Gotthardt, K., Guerrero-Castillo, S., and Brandt, U. (2016). Evolution and structural organization of the mitochondrial contact site (MICOS) complex and the mitochondrial intermembrane space bridging (MIB) complex. Biochim. Biophys. Acta *1863*, 91–101.

Supplementary Information & Methods

Cristae formation is a mechanical buckling event controlled by the inner membrane lipidome

Kailash Venkatraman, Christopher T. Lee, Guadalupe C. Garcia, Arijit Mahapatra, Guy Perkins, Keun-Young Kim, H. Amalia Pasolli, Sebastien Phan, Jennifer Lippincott-Schwartz, Mark Ellisman, Padmini Rangamani, and Itay Budin

Contents:

Supplementary Figures

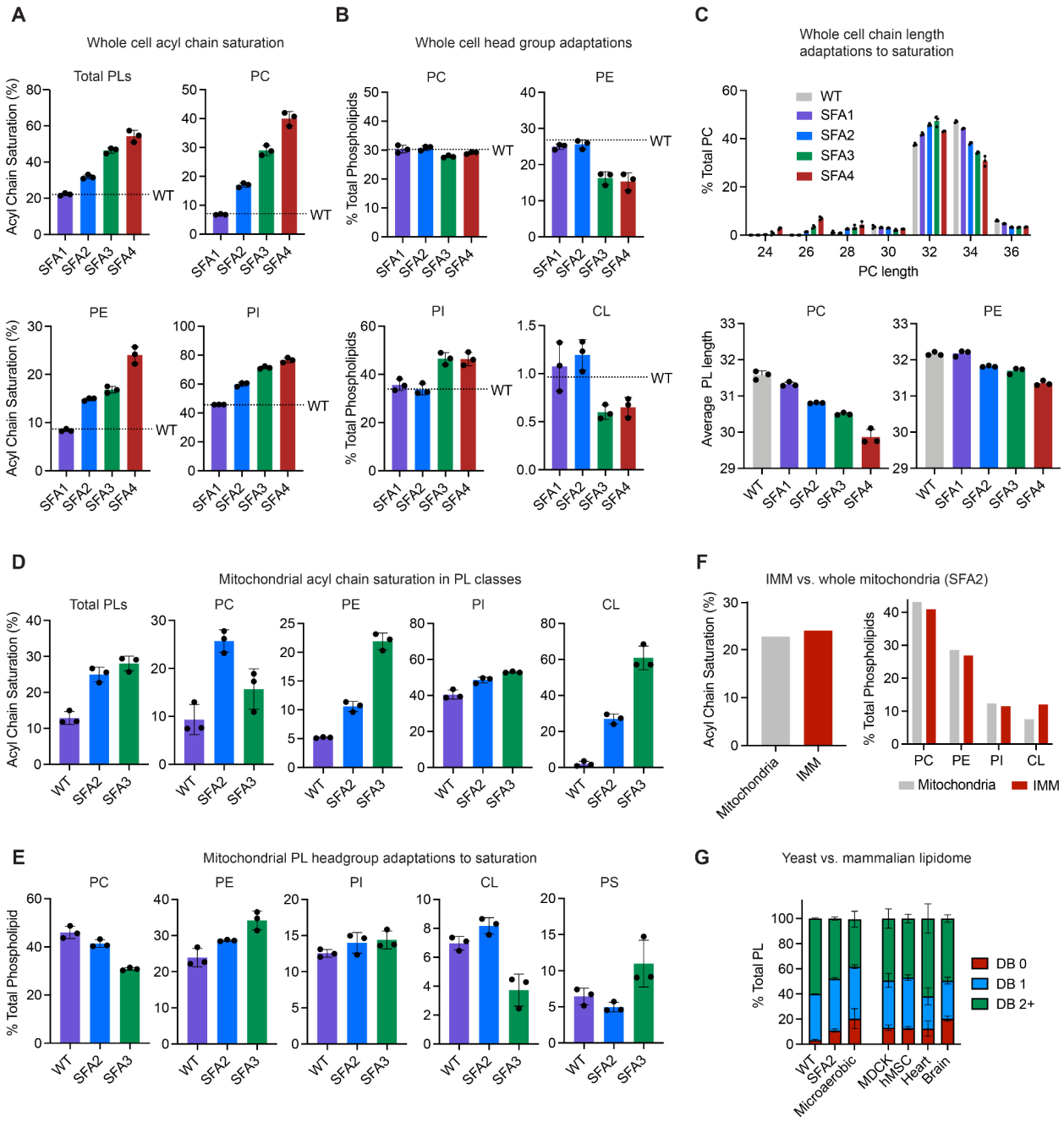

Figure S1: Changes to whole cell and mitochondrial lipid profile upon modulation of Ole1p expression.

(A) Decreasing Ole1p expression increases the acyl chain saturation of the total yeast PL pool, and major PL classes as assayed by lipidomics, error bars indicate SD, n=3 independent cultures. WT levels are shown as dotted lines.

(B) Potentially compensatory changes to the whole cell lipidome in response to increasing saturation. Shown are the abundance of major yeast PLs in SFA strains, n=3 independent cultures. WT levels shown as dotted lines. As saturation increases, PE and CL decrease, while PI increases. Error bars indicate SD.

(C) Increasing lipid saturation results in shortening of PC and PE acyl chains in the whole cell. Shown are the sum of the lengths for the *sn*-1 and *sn*-2 chains.
(D) Acyl chain saturation in isolated mitochondria from SFA strains and WT as determined by intact lipid analysis for the total PL pool, n=3 independent cultures. Error bars indicate SD.
(E) PL headgroup adaptations in isolated mitochondria from SFA strains and wild-type in major PL classes as determined by lipidomic analysis, n=3 independent cultures. In the mitochondria, PC decreases and PE increases as saturation increases. Error bars indicate SD.
(F) The IMM and whole mitochondrial lipidome display similar levels of saturation and PE/PC, but differ in abundance of CL (higher in the IMM).
(G) Mammalian lipidomes contain similar lipid saturation profiles to yeast SFA2 and micro-aerobically grown cells, where CL is essential. Shown is the double bond profile of all PLs as determined through lipidomics from *S. cerevisiae* (this study) in comparison with mammalian cell lines (MDCK-CM and hMSC-CM) and isolated tissues previously analyzed using the same lipidomics platform[140]. WT yeast grown under vigorous aeration have a low number of saturated and monounsaturated PLs, while WT cells grown under physiologically-relevant oxygen concentrations (microaerobic) or engineered strains (SFA2) show profiles more similar to mammalian cells. In the latter systems, CL is an essential component for proper mitochondrial biogenesis. Error bars indicate SD.

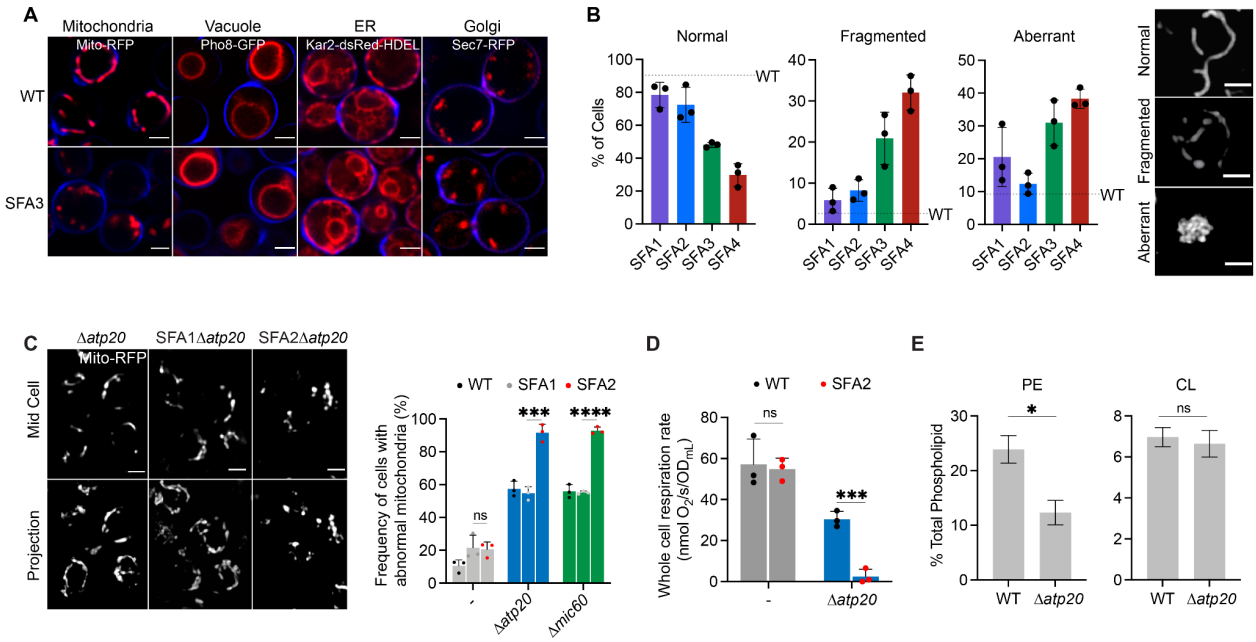

Figure S2: Effects of PL saturation on organelle morphology and its interactions with cristae shaping proteins.

(A) Decreasing expression of Ole1p expression results in abnormal mitochondria in SFA3 while other organelles remain intact. Organelles were imaged in cells that were transformed with plasmids expressing the following fusion proteins: mts-RFP (Mitochondria), Pho8-GFP (Vacuole), Kar2-dsRed-HDEL (ER), Sec7-RFP (Golgi). Cells were grown to exponential phase and were stained with cell wall-binding calcofluor white (blue). Scale bars, 2 μm.

(B) Imaging of matrix-localized mito-RFP was used to quantify the frequency of mitochondrial abnormality as a function of the amounts of normal, fragmented and aberrant mitochondria. Normal mitochondria contain tubulations throughout the whole yeast cell, while fragmented mitochondria retain an overall mitochondrial structure but have lost the interconnected tubular network associated with normal mitochondria. Aberrant mitochondria are characterized by punctate aggregations of mitochondria in the center of the yeast cell. Cells were imaged in n=3 independent cultures. Error bars indicate SD. Scale bars, 2 μm.

(C) Representative Airyscan confocal micrographs of yeast expressing matrix-localized RFP (mts-RFP). (Right) Frequency of mitochondrial abnormalities as assayed by analysis of mts-RFP. N>50 cells were counted in biological triplicate (n=3) in each condition. Error bars indicate SD. ***p=0.0006, ****p <0.0001 unpaired two-tailed t-test compared SFA2Δ*atp20* and SFA2Δ*mic60* against SFA1Δ*atp20* and SFA1Δ*mic60* respectively.

(D) Respiration rates in Δ*atp20* and SFA2Δ*atp20* cells measured in biological triplicate (n=3) using a Clark electrode. Error bars represent SD. ***p < 0.0005, unpaired two-tailed t-test compared against Δ*atp20*.

(E) Lipidomics on isolated Δ*atp20* mitochondria reveals decreased levels of PE while the levels of CL remain the same. Error bars indicate SD.

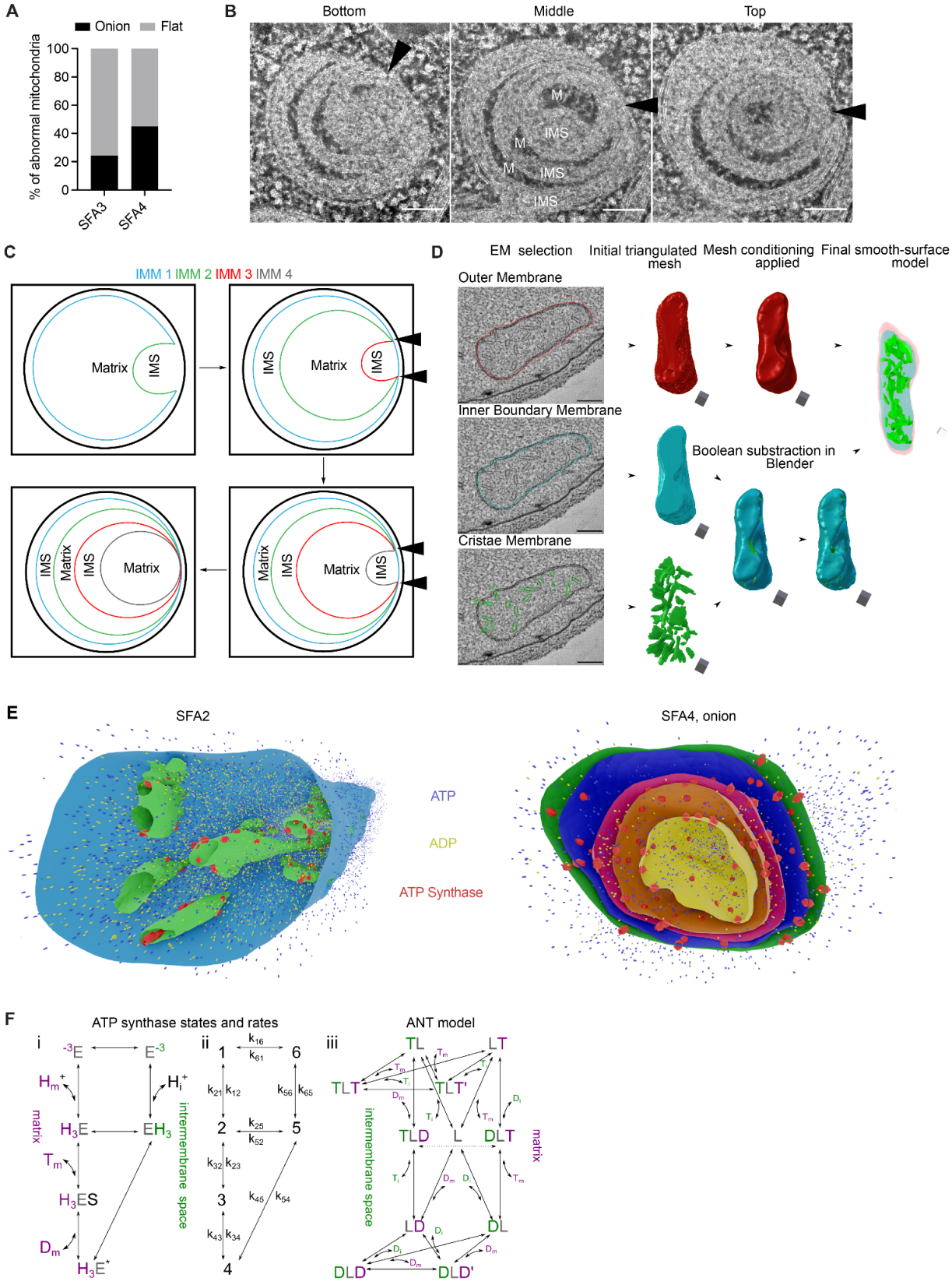

Figure S3: Multi-tilt tomography and analysis of subsequent reconstructions reveals a potential mechanism for loss of ATP production in onion-like mitochondria.

(A) Quantitative analysis of thin-section TEM micrographs reveals the abnormal mitochondria in SFA3 are predominantly flat, while in SFA4 there is an even distribution of onion and flat abnormal mitochondria. At least N=40 mitochondria were quantified from each strain.
(B) Multi-tilt tomogram slices of HPFS SFA4 yeast cells at three z-positions. 'M' indicates matrix regions (dark), while 'IMS' indicates intermembrane space regions (light). Shading indicates alternating matrix and IMS regions, as previously observed[19]. Black triangles indicate observed regions of contact points between IMM layers, suggesting a continuous IMM. Scale bars, 100 nm.
(C) Schematic depiction for one model of how onion-like morphology could be formed by a continuous IMM undergoing subsequent buddings. Black triangles indicate regions of contact points between multiple apparent IMM layers.
(D) Example of Blender-based 3D Mesh generation pipeline from EM tomograms.
(E) Snapshots of ATP generation simulations as displayed in Movie S4 and S5. SFA2 shows localizations of ATP synthases to regions of high curvature in CMs, while in the SFA4 onion ATP synthases are distributed evenly on each layer of IMM based on previous cryo electron tomography reconstructions.
(F) (i-iii) Schematic representations of the kinetic states and modeled rates of ATP synthase and ANT used to construct the metabolic model. Further details of the model can be found in the Supplementary Text.

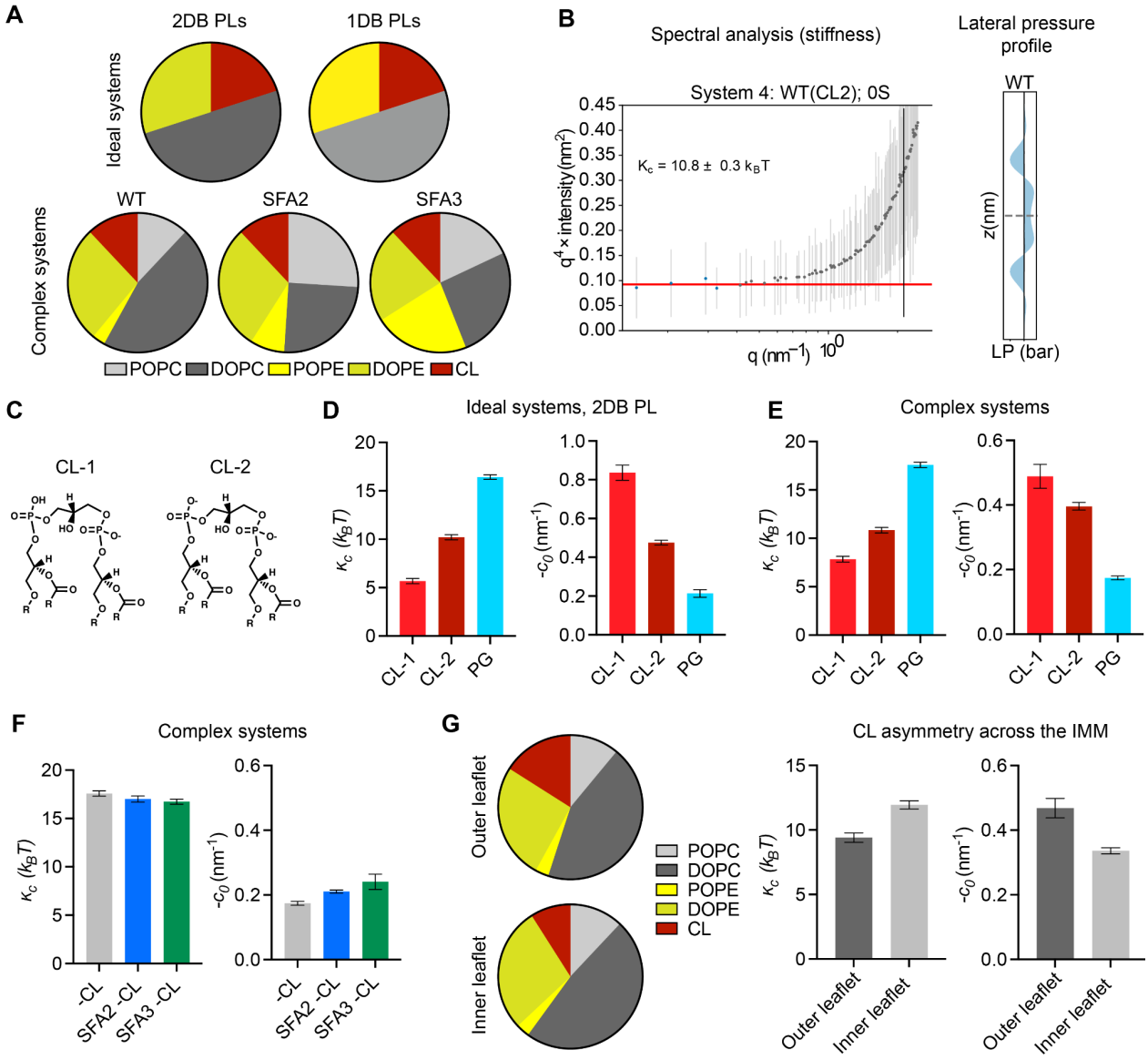

Figure S4: Coarse-grained molecular dynamics predicts an important role for CL in shaping membrane mechanical properties.

(A) Ideal systems contained lipid compositions of fixed abundance, while changing the unsaturation of the acyl chains from di-unsaturated to monounsaturated. In contrast, the 'complex' systems mimicking the mitochondrial lipidomes of SFA strains accounted for headgroup adaptations to increasing saturation, such as increasing PE. Full compositions are listed in Table S2.

(B) Example spectral analysis of thermal undulations, used to calculate bending moduli, and lateral pressure profiles, used to calculate spontaneous curvature.

(C) Chemical structures of CL in dianion (CL-2) and monoanion (CL-1) ionization states.

(D) In ideal systems, the changing of ionization state of CL from -1 to -2 causes a minor increase in membrane stiffness and a major reduction in spontaneous curvature. Absence of CL increases membrane stiffness and reduces spontaneous curvature as determined through MARTINI CG-MD.

(E) Accounting for headgroup adaptations in complex systems, simulations still show the same trend with dianionic CL and loss of CL showing increases in membrane stiffness and a reduction in spontaneous curvature.
(F) While increasing lipid saturation has a minimal effect on membrane stiffness in the absence of CL, the increase in the magnitude of spontaneous curvature suggests that the presence of PE can partially, but not completely, compensate for loss of curvature provided by CL.
(G) Modeling of outer leaflet enrichment of CL in the yeast IMM. Simulated changes in CL concentrations reported in Gallet et. al[102] results in membrane softening and increased spontaneous curvature. Two sets of simulations were set up with the estimated compositions of the outer and inner IMM leaflets shown in the pie charts. The simulated outer membrane systems were softer (lower stiffness) and had a larger negative spontaneous curvature. The difference in the outer and inner leaflet curvatures was 0.1±0.04 nm^{-1}, which is an estimation for asymmetry-induced c_0.

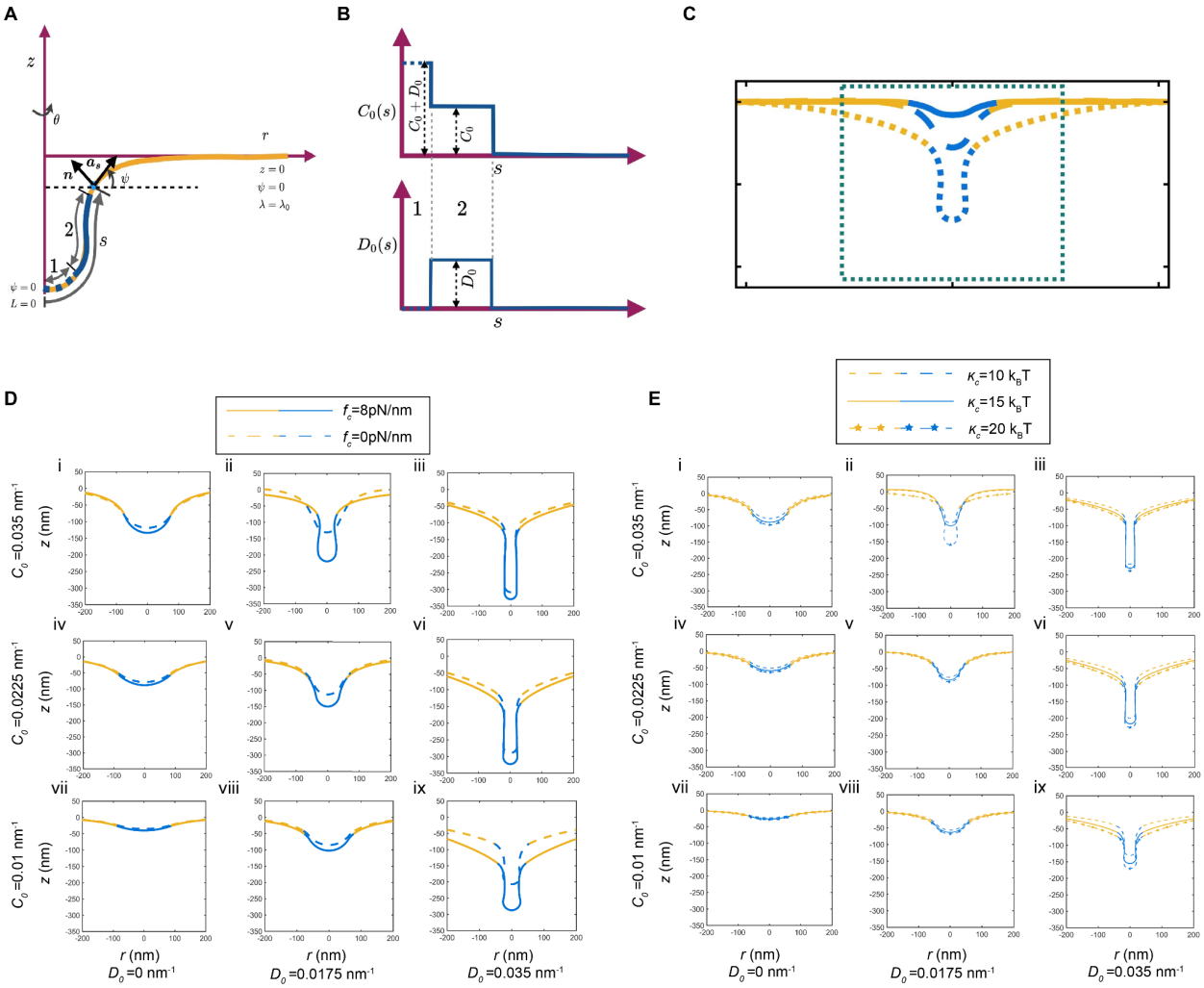

Figure S5: Continuum modeling details and comparison of tubular morphologies with and without an applied collar force.

(A) Schematic showing the axisymmetric membrane configuration along with the boundary conditions. The yellow regions depict the bare lipid bilayer, and the blue regions depict the regions where different spontaneous curvatures are prescribed.

(B) Prescription of isotropic and anisotropic spontaneous curvature along the arc length in the simulations.

(C) The simulation domain is large to avoid boundary effects but the zoomed in portion in the dashed box is shown to demonstrate the shapes of the membrane.

(D) Comparison of the tubular shapes with (solid lines) and without (dashed line) the collar force at the base of the cristae. All parameters are the same as those in Figure 5B. Presence of a collar force promoted cristae like structures for the same values of imposed curvatures. This is particularly apparent in panel ii.

(E) Shapes of the membrane for the same values of coat area, collar force, and variations in the isotropic and anisotropic spontaneous curvature as panel D for different values of bending modulus. We observe that the shapes of the tubular cristae are not sensitive to changes in bending modulus for low curvature values but differences in membrane curvature can be seen for high values of isotropic and anisotropic spontaneous curvatures.

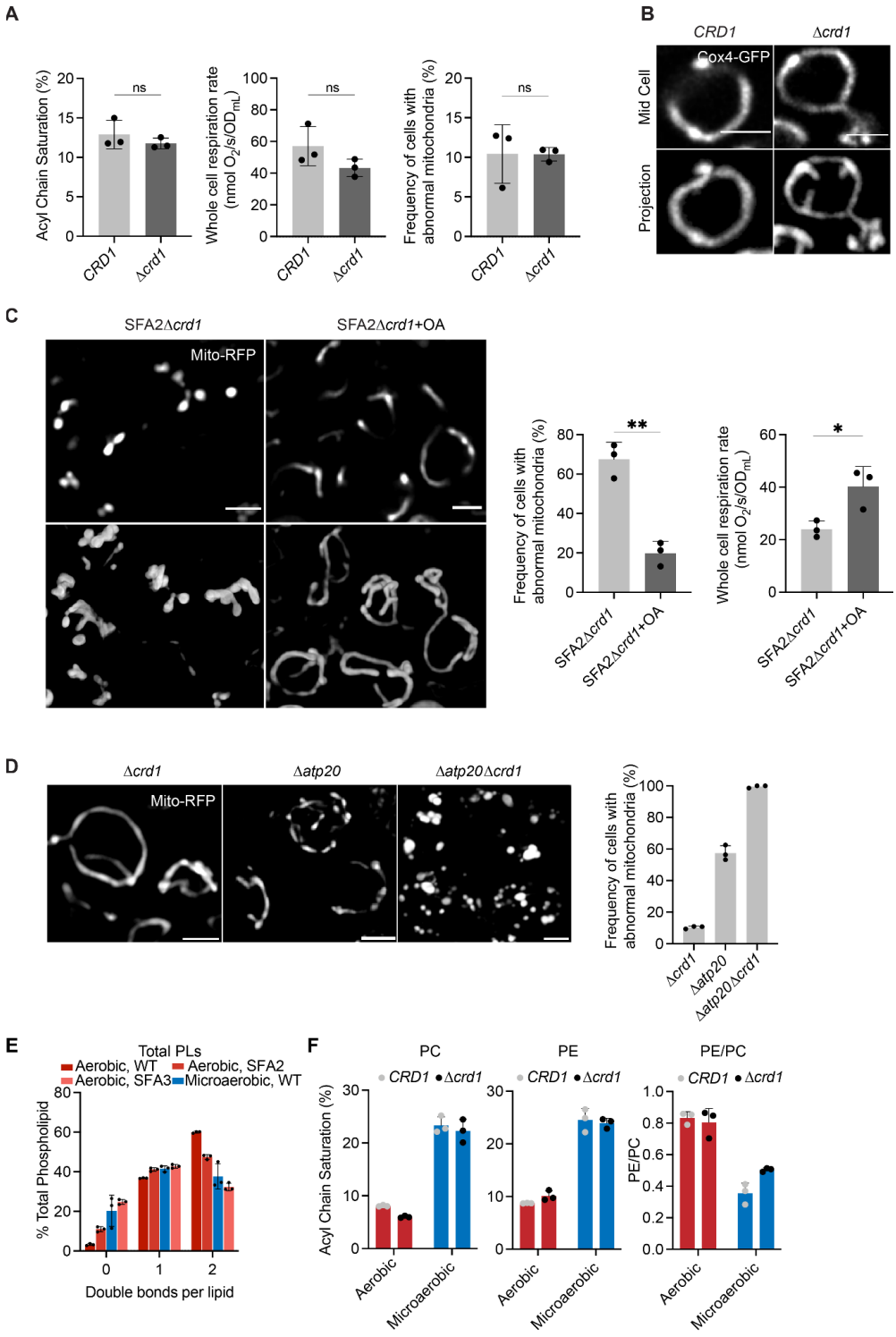

Figure S6: Roles for CL synthesis in shaping mitochondrial morphology.
(A) Mitochondrial PL saturation, respiration rate and mitochondrial abnormality measurements of *CRD1* and Δ*crd1* cells. PL saturation was computed from lipidomics analysis on isolated mitochondria. Respiration measurements were performed using Clark electrode, and mitochondrial abnormalities were determined using confocal microscopy with yeast expressing a

matrix-localized mts-RFP (N>50 cells quantified per replicate). Measurements were taken from independent cultures (n=3), error bars indicate SD.

(B) Airyscan confocal micrographs of aerobic wild-type and Δ*crd1* expressing IMM protein Cox4-GFP. Scale bars, 2 μm. Line profile analysis (below) depicts fluorescent intensity across the indicated mitochondria.

(C) Representative Airyscan confocal micrographs of SFA2Δ*crd1* yeast, grown in the presence and absence of OA, expressing mts-RFP. Scale bars, 2 μm. **p < 0.005, unpaired two-tailed t-test compared against SFA2Δ*crd1*. Respiration rates of SFA2Δ*crd1* cells in the presence and absence of OA were measured in biological replicates (n=3) using a Clark electrode. Error bars indicate SD. *p < 0.05 unpaired two-tailed t-test.

(D) Loss of CL and ATP synthase dimerization results in complete ablation of mitochondrial morphology and structure as assayed by analysis with mts-RFP. N>50 cells were counted in biological triplicate (n=3) in each condition. Error bars indicate SD. Individual deletion of Crd1p results in normal mitochondrial morphology while half of the cells in Δ*atp20* still retain normal morphology. Scale bars, 2 μm.

(E) Lipidomic analysis of the double bond distribution of microaerobic yeast (n=3) shows decreased di-unsaturated PL chains and increased saturated PL chains. This is consistent with an intermediary increase in PL saturation between SFA2 and SFA3 levels. Error bars indicate SD.

(F) The major cellular PL classes, PC and PE, show increased lipid saturation under microaerobic conditions. Also shown is the decrease in whole cell PE/PC ratio under microaerobic conditions, as observed in SFA strains (Figure 3D).

Supplementary Tables

Table S1A: Bending moduli (κ_c) values extracted from X-ray scattering analysis or micropipette aspiration analysis of PC membranes as a function of acyl chain saturation.

X-ray scattering

Lipid	Acyl Chains	κ_c (10^{-20} J)	Source
POPC	16:0 18:1	8.5	[141]
DOPC	18:1 18:1	8.5±0.6	[142]

Micropipette aspiration

Lipid	Acyl Chains	κ_c (10^{-19} J)	Source
SOPC	18:0 18:1	0.90±0.06	[84]
DOPC	18:1 18:1	0.85±0.10	[84]

Table S1B: Bending moduli (κ_c) values extracted from MD simulations of PE as a function of acyl chain saturation.

Lipid	Acyl Chains	κ_c (10^{-20} J)	Source
POPE	16:0 18:1	13.3±0.6	[76]
DOPE	18:1 18:1	11.8±0.3	[76]

Table S1C: Spontaneous curvature (c_0) values extracted from SAXS analysis of PC and PE lipids as a function of acyl chain saturation.

PC

Lipid	Acyl Chains	Matrix	c_0 (nm^{-1})	Source
DPPC	16:0 16:0	DOPE	0.05±0.05	[143]
POPC	16:0 18:1	DOPE	0.01±0.04	[143]
DOPC	18:1 18:1	DOPE	-0.04±0.04	[143]

PE

Lipid	Acyl Chains	Matrix	c_0 (nm^{-1})	Source
POPE	16:0 18:1	-	-0.317±0.007	[144]
DiPoPE	16:1 16:1	-	-0.382±0.009	[144]
DOPE	18:1 18:1	-	-0.409±0.010	[144]

Table S2: List of membrane compositions simulated by CG-MD; the number of lipids for each type are shown.

System name	POPC	DOPC	POPE	DOPE	CDL1	CDL2	POPG	DOPG
1:Complex WT (CL-1)	648	2486	162	1460	648	0	0	0
2: Complex SFA2 (CL-1)	1406	1352	432	1568	648	0	0	0
3: Complex SFA3 (CL-1)	972	1406	1188	1188	648	0	0	0
4: Complex WT (CL-2)	648	2486	162	1460	0	648	0	0
5: Complex SFA2 (CL-2)	1406	1352	432	1568	0	648	0	0
6: Complex SFA3 (CL-2)	972	1406	1188	1188	0	648	0	0
7: Complex WT (PG)	540	2974	108	1188	0	0	324	270
8: Complex SFA2 (PG)	1080	1838	378	1352	0	0	648	108
9: Complex SFA3 (PG)	918	1406	1188	1134	0	0	648	108
10: Ideal DOPL (CL-1)	0	2704	0	1622	1080	0	0	0
11: Ideal POPL (CL-1)	2704	0	1622	0	1080	0	0	0
12: Ideal DOPL (CL-2)	0	2704	0	1622	0	1080	0	0
13: Ideal POPL (CL-2)	2704	0	1622	0	0	1080	0	0
14: Ideal DOPL (PG)	0	2704	0	1622	0	0	0	1080
15: Ideal POPL (PG)	2704	0	1622	0	0	0	0	1080
16: Outer IMM leaflet (CL-1)	594	2378	162	1406	864	0	0	0
17: Inner IMM leaflet (CL-1)	648	2594	162	1514	486	0	0	0
18: Outer IMM leaflet (CL-2)	594	2378	162	1406	0	864	0	0
19: Inner IMM leaflet (CL-2)	648	2594	162	1514	0	486	0	0
20: Pure CL-1	0	0	0	0	5408	0	0	0
21: Pure CL-2	0	0	0	0	0	5408	0	0

Table S3: Strains used in this study

Experimental Models: Organisms/strains

Reagent or Resource	Source	Description
W303a (*MATa leu2-3112 trp1-1 can1-100 ura3-1 ade2-1 his3-11,15*)	ATCC	Haploid background strain
W303a, *ole1::Pm1-OLE1*	This study	Weak constitutive promoter driving *OLE1* expression (SFA4)
W303a, *ole1::Pm2-OLE1*	This study	Weak constitutive promoter driving *OLE1* expression (SFA3)
W303a, *ole1::Pm3-OLE1*	This study	Medium strength constitutive promoter driving *OLE1* expression (SFA2)
W303a, *ole1::Pm4-OLE1*	This study	Strong constitutive promoter driving *OLE1* expression (SFA1)
W303a, *ole1::Pm1-OLE1* Δ*crd1*::KanMX6	This study	SFA4Δ*crd1*
W303a, *ole1::Pm2-OLE1* Δ*crd1*::KanMX6	This study	SFA3Δ*crd1*
W303a, *ole1::Pm3-OLE1* Δ*crd1*::KanMX6	This study	SFA2Δ*crd1*
W303a, *ole1::Pm4-OLE1* Δ*crd1*::KanMX6	This study	SFA1Δ*crd1*
W303a, Δ*crd1*::KanMX6	This study	
W303a, Δ*atp20*::His3	This study	
W303a, *ole1::Pm4-OLE1* Δ*atp20*::His3	This study	SFA1Δ*atp20*
W303a, *ole1::Pm3-OLE1* Δ*atp20*::His3	This study	SFA2Δ*atp20*
W303a, Δ*mgm1*::His3	This study	
W303a, Δ*mic60*::His3	This study	
W303a, *ole1::Pm4-OLE1* Δ*mic60*::His3	This study	SFA1Δ*mic60*
W303a, *ole1::Pm3-OLE1* Δ*mic60*::His3	This study	SFA2Δ*mic60*

Table S4: Plasmids used in this study

Plasmid	Source	Description
pPW1882	Dr. Peter Walter	Mitochondrial matrix RFP

pPW1409	Dr. Peter Walter	ER-localized RFP
pRS416	Dr. Arnold Seo	Vacuole Pho8 GFP
pSEC7-RFP	Dr. Arnold Seo	Early Golgi-RFP
Cox4-GFP	Dr. Zhiping Xie	CIV subunit 4 IMM localized-GFP

Table S5: Antibodies used in this study

Reagent or Resource	Source	Description
Anti-ATP synthase subunit β antibody	Dr. Alexander Tzagoloff	Goat, polyclonal[145]

Multimedia file captions

Movie S1: Animation depicting the mean curvature map within the IMM of a cristae-containing SFA2 mitochondrion.

Movie S2: Animation depicting the mean curvature map within the flat IMM of a SFA4 mitochondrion.

Movie S3: Animation depicting the mean curvature map within the IMM of an onion-like SFA4 mitochondrion.

Movie S4: Animation depicting the simulated distribution of ATP synthases (large red spheres), ANTs, ATP (small blue spheres) and ADP (small yellow spheres) within the IMM of a cristae-containing SFA2 mitochondrion.

Movie S5: Animation depicting the simulated distribution of ATP synthases (large red spheres), ANTs, ATP (small blue spheres) and ADP (small yellow spheres) within the IMMs of an onion-like SFA4 mitochondrion.

Movie S6: Animation showing the change in the shape of membrane for bending modulus 15 k_BT, with collar force 8 pN/nm, and D_0 fixed at 0.0175 nm^{-1}. The movie shows the shape as C_0 increases.

Movie S7: Animation showing the change in the shape of membrane for bending modulus 15 k_BT, with collar force 8 pN/nm, and C_0 fixed at 0.0225 nm^{-1}. The movie shows the shape as D_0 increases.

Experimental Procedures

Strains and growth media

The yeast strains used in this study can be found in Table S3. Yeast cells were grown in YPEG (1% Bacto yeast extract, 2% Bacto peptone, 2% Ethanol, 2.5% Glycerol), YPD medium (1% Bacto yeast extract, 2% Bacto peptone, 2% glucose) or complete supplement mixture (CSM, 0.5% Ammonium Sulfate, 0.17% yeast nitrogen base without amino acids and 2% glucose) lacking appropriate amino acids for selection. Yeast mutants were generated by PCR-based homologous recombination, ORFs of the gene of interest were replaced by either *KanMX* or *His3MX6* cassettes. For *OLE1* promoter substitution, a set of previously generated mutant *TEF1* promoters were utilized[146]. An additional, weaker promoter (*Pm1)* was generated by error prone PCR and added to this set. Promoter substitution was completed on the haploid base strain W303a as previously described[147].

Yeast physiology

Growth on non-fermentable carbon sources were assayed using growth curves on 24-well plates (Avantor) sealed with a gas permeable film (Diversified Biotech). Cells were first grown in biological triplicate overnight in complete synthetic medium (CSM) containing 2% glucose. Cells were back-diluted 1:100 in fresh CSM containing 2% glucose or 3% glycerol and shaken in a plate reader (Tecan) for 48 hours. Specific growth rates were extracted from the exponential phase of growth. For viability assays, cells were first grown in the same fashion as for yeast growth curves but were serially diluted onto CSM plates (1:5 successive dilutions) containing either 2% glucose or 3% glycerol and 2% ethanol. Plates were grown for 3 days on glucose plates, and for 4 days for ethanol/glycerol plates.

For microaerobic growth, cells were pre-incubated overnight in CSM without uracil (2% glucose) in a controlled temperature shaker at 30°C. Cells were then back diluted into fresh synthetic medium and grown to stationary phase in home-built microaerobic chambers with limited oxygen supply. Chambers consisted of glass culture tubes with tight fitting rubber caps; tubing allowed for gas efflux into an attached bubbler. Live cell imaging was conducted on aliquots, and cell pellets were resuspended in sterile water, lysed and flash frozen for lipidomics analysis.

Lipidomics

Lipid compositions of whole cells and isolated mitochondria from yeast strains were conducted at Lipotype GmbH (Dresden, Germany). Mass spectrometry-based lipid analysis was performed as previously described[148,149]. Lipids were extracted using a two-step chloroform/methanol procedure[148]. Samples were spiked with internal lipid standard mixture containing: CL 14:0/14:0/14:0/14:0, ceramide 18:1;2/17:0 (Cer), diacylglycerol 17:0/17:0 (DAG), lyso-phosphatidate 17:0 (LPA), lyso-phosphatidyl-choline 12:0 (LPC), lysophosphatidylethanolamine 17:1 (LPE), lyso-phosphatidylinositol 17:1 (LPI), lysophosphatidylserine 17:1 (LPS), phosphatidate 17:0/14:1 (PA), phosphatidylcholine 17:0/14:1 (PC), PE 17:0/14:1, PG 17:0/14:1, PI 17:0/14:1, phosphatidylserine 17:0/14:1 (PS), ergosterol ester 13:0 (EE) and triacylglycerol 17:0/17:0/17:0 (TAG). After extraction, the organic phase was transferred to an infusion plate and dried in a speed vacuum concentrator. 1st step dry extract was re-suspended in 7.5 mM ammonium acetate in chloroform/methanol/propanol (1:2:4, v:v:v) and 2nd step dry extract in 33% ethanol solution of methylamine in chloroform/methanol (0.003:5:1; v:v:v). All liquid handling steps were performed using Hamilton Robotics STARlet robotic platform with the Anti Droplet Control feature for organic solvents pipetting. Samples were analyzed by direct infusion on a QExactive mass spectrometer (Thermo Scientific)

equipped with a TriVersa NanoMate ion source (Advion Biosciences). Samples were analyzed in both positive and negative ion modes with a resolution of $R_{m/z=200}$=280000 for MS and $R_{m/z=200}$=17500 for MSMS experiments, in a single acquisition. MSMS was triggered by an inclusion list encompassing corresponding MS mass ranges scanned in 1 Da increments[150]. Both MS and MSMS data were combined to monitor EE, DAG and TAG ions as ammonium adducts; PC as an acetate adduct; and CL, PA, PE, PG, PI and PS as deprotonated anions. MS only was used to monitor LPA, LPE, LPI and LPS as deprotonated anions; Cer and LPC as acetate adducts. Data were analyzed with in-house developed lipid identification software based on LipidXplorer[151,152]. Data post-processing and normalization were performed using an in-house developed data management system. Only lipid identifications with a signal-to-noise ratio >5, and a signal intensity 5-fold higher than in corresponding blank samples were considered for further data analysis.

Mitochondria purification

Yeast mitochondria were isolated from 1L of yeast cells grown in YPEG (1% Bacto yeast extract, 2% Bacto peptone, 2% Ethanol, 3% Glycerol) or YPD medium (1% Bacto yeast extract, 2% Bacto peptone, 2% glucose) at 30°C as previously described[153,154]. Cells were grown to stationary phase and harvested in a buffer consisting of 100mM Tris/H_2SO_4 (pH 9.4) and 10mM dithiothreitol. Spheroplasts were formed from digestion of the cell wall using Zymolyase 20-T (MP Biomedicals) in a buffer containing 20mM Potassium Phosphate (pH 7.4) and 1.2M Sorbitol. Spheroplasts were lysed by homogenization using a glass homogenizer and subsequently centrifuged to remove unbroken cells, large debris and nuclei. Enriched mitochondria were pelleted and resuspended in SEM buffer (10mM MOPS/KOH (pH 7.2), 250mM Sucrose and 1mM EDTA), snap frozen and stored for up to 1 month at -80 °C. To obtain purified mitochondria, bereft of contamination from other organelles, such as microsomes, Golgi and vacuoles, the crude mitochondrial fraction is subjected to a sucrose density cushion ultracentrifugation. Cushions are poured containing 60% and 32% (w/v) sucrose concentrations in EM buffer (10mM MOPS/KOH (pH 7.2), 1mM EDTA). Density cushions containing crude mitochondrial samples in SEM buffer are subjected to ultracentrifugation in a SW32 Ti swinging-bucket rotor for 1 hour at 100,000 x g at 4 ºC. The yellow/brown band at the 60/32% (w/v) sucrose interface is removed and centrifuged to pellet purified mitochondria for subsequent analysis. Mitochondrial protein quantity was determined via BCA assay.

Mitoplasts containing an intact inner mitochondrial membrane stripped of the outer membrane were isolated as previously described[55]. After initial incubation of isolated mitochondria in a hypotonic buffer followed by centrifugation for 10 minutes at 14,000 x g at 4 ºC. Mitoplasts were resuspended in SEM buffer prior to lipidomic analysis.

Respirometry

Oxygen consumption rates (OCR) of whole cell yeast strains were measured with a Clark electrode (YSI 5300A Biological Oxygen Monitor System). Cells were grown in biological replicates overnight in CSM containing 0.4% glucose (starvation conditions). Cells were then back-diluted into fresh CSM and grown to OD 0.4-0.6. OCRs were quantified after initial stirring of culture for 3 minutes in a thermostatically controlled chamber at 30 °C. Respiration rates were determined after normalization to OD of the sample.

Live cell microscopy

To assess mitochondrial morphology, cells were initially grown in biological replicates overnight in CSM containing 0.4% glucose under selection conditions. Cells were then back diluted and imaged in an exponential phase. Prior to imaging, cells were plated on 8 well chambered coverglass (Nunc Lab-Tek, Thermo Fisher Scientific) pre-incubated with concanavalin A (MP Biomedicals). Live cell microscopy was conducted using Plan-Apochromat

63x/1.4 Oil DIC M27 on the Zeiss LSM 880 with Airyscan (default processing settings); image acquisition and processing were performed using ZEN software.

For image analysis, cells were split into 3 groups based on mitochondrial morphology: 'aberrant' groups display a punctate cluster at the center of the cell, whilst 'fragmented' groups display a lack of tubular morphology and consist of individual mitochondrial puncta separated within the cell (Figure S2B). Normal mitochondrial morphology is associated with tubes spanning the length of the cell that display regular lateral motion. Percentage 'mitochondrial abnormality' is derived from combining the amount of cells with an aberrant or fragmented morphology divided by the total number of cells. At least 50 cells were quantified in a given sample and replicates were of individually grown cultures. To visualize the yeast cell wall, cells were stained with calcofluor white (Sigma-Aldrich), which is able to bind chitin within the cell wall.

Membrane potential was assayed by imaging of cells stained with Tetramethylrhodamine, ethyl ester (TMRE, Thermo Fisher Scientific T669). Cells were first grown to exponential phase in CSM containing 0.4% glucose and stained with 200nM TMRE for 20 minutes. Cells were then washed twice with water prior to imaging on the Zeiss LSM 880 with Airyscan, using a 561 nm laser line with 1% laser power. For analysis of membrane potential in uncoupled conditions, cells were incubated with 20 μM carbonyl cyanide m-chlorophenyl hydrazone (CCCP, Sigma-Aldrich) for 10 minutes prior to incubation with TMRE. For analysis of membrane potential in ATP synthase inhibited conditions, cells were incubated with 5 μM oligomycin for 45 minutes prior to incubation with TMRE. Peak intensities were quantified from at least 10 cells in each condition.

Blue Native-PAGE analysis

Isolated mitochondria solubilized in digitonin (0.5:1 g/g protein) were assayed by BN-PAGE as previously described[155], with minor modifications. 200-400 μg of mitochondria were incubated with digitonin for 10 minutes prior to centrifugation at 20,000 x g for 30 mins at 4 ºC. The subsequent supernatant was mixed with native PAGE buffer and glycerol and loaded onto precast native PAGE gels (Invitrogen). ATP synthase dimerization state was probed using β-ATP synthase primary antibody (1:1000) and anti-rabbit IgG secondary antibody (Thermo Fisher Scientific).

Electron Microscopy

Blocks of late exponential phase yeast cells were prepared either by high-pressure freezing/freeze substitution (HPF-FS)[156] (SFA4, SFA2Δ*crd1*, Δ*atp20*,) or chemical fixation followed by partial cell wall digestion[157] (SFA2, SFA4, Δ*crd1* and microaerobic cells) as previously described. Cell wall digestion was required for high contrast staining of WT-like tubular CM for 3D segmentation. For microaerobic cells, chemical digestion was performed with 0.25 mg/mL zymolyase-20T for one hour at room temperature. Aerobically-grown mutant cells lacking CMs showed sufficient membrane contrast in HP-FS samples. Thin sections about 60 nm thick were cut from the blocks of yeast with a Leica ultramicrotome and placed on 200-mesh uncoated thin-bar copper grids. A Tecnai Spirit (FEI, Hillsboro, Oregon) electron microscope operated at 120 kV was used to record images with a Gatan Ultrascan 4K x 4K CCD camera at 6.0, 2.9, and 1.9 nm/pixel.

Tomography

Semi-thick sections of thickness about 300 nm were cut from the blocks of yeast with a Leica ultramicrotome and placed on 200-mesh uncoated thin-bar copper grids. 20-nm colloidal gold particles were deposited on each side of the grid to serve as fiducial cues. The specimens were irradiated for about 20 min to limit anisotropic specimen thinning during image collection at the magnification used to collect the tilt series before initiating a dual-axis tilt series. During data

collection, the illumination was held to near parallel beam conditions and the beam intensity was kept constant. Tilt series were captured using SerialEM (University of Colorado, Boulder) software on a Tecnai HiBase Titan (FEI) electron microscope operated at 300 kV and 0.81 nm/pixel. Images were recorded with a Gatan 4K x 4K CCD camera. Each dual-axis tilt series consisted of first collecting 121 images taken at 1 degree increment over a range of -60 to +60 degrees followed by rotating the grid 90 degrees and collecting another 121 images with the same tilt increment. To improve the signal-to-noise ratio, 2x binning was performed on each image by averaging a 2x2 x-y pixel box into 1 pixel using the newstack command in IMOD (University of Colorado, Boulder). The IMOD package was used for tilt-series alignment, reconstruction, and volume segmentation. R-weighted back projection was used to generate the reconstructions.

Mesh Generation and Analysis

3D *in silico* reconstructions of mitochondria were generated from electron-tomographic images. The software IMOD was used to trace the mitochondrial membranes in 2D: the outer leaflet of the OM, and the inner leaflet of the IBM and CM were manually traced as separate objects, following procedures previously described[7]. Subsequently, 2D traces were imported into Blender using the NeuropilTools module in CellBlender. The program Contour Tiler[158] — integrated with NeuropilTools — was used to generate 3D triangulated meshes in Blender. The triangulation was performed individually for each membrane object in each mitochondrion. Afterwards, the Boolean Difference Modifier was used to subtract the CM object from the IBM object, generating in this manner the CJs in the IBM. The meshes were refined with the Smooth and Normal Smooth improvement tools from GAMer2[91]. Curvature calculations were carried out with GAMer2, using the MDSB algorithm. For all curvature analysis, the smooth curvature after one iteration was considered. This smoothing represents the average curvature of a vertex and its neighbors. Surface areas and volumes were calculated using the CellBlender add-on in Blender.

Modeling Procedures

ATP production modeling

The computational for ATP generation in mitochondria is based on previous modeling efforts [97,159–162]. We solve the reactions (detailed below) using MCell [163] to accurately capture the stochastic nature of the events underlying ATP production in the small volumes of the mitochondria. The model has a total of 19 equations and 41 parameters and the thermodynamic details are given in [159]. We briefly describe the main components of the model below.

ATP synthase: The ATP synthase model is composed of ATP synthase (represented as E) that can be in six states (Figure S3F), representing different protein configurations. Each state corresponds with a number from 1 to 6, and each transition has associated a rate constant k_{ij} (transition from the state i → j). In some cases k_{ij} depends on the membrane potential, proton concentration, or phosphate concentration. The list of reactions and model parameters are given below, reproduced from[159]. The model was adapted from the work of Pietrobon and Caplan[164].

ATP synthase is modeled as a membrane protein that can transport protons (H^+) from and to the matrix and synthesize ATP. The translocation of 3 H^+ is coupled to the phosphorylation of one ADP into ATP, approximating the stoichiometry of the yeast ATP synthase with a c_{10} ring (10 H^+/ 3 ATP). The free enzyme with its negative charged cavity facing the IMS is represented by E^{-3}. Three protons can bind, generating the transition to state EH_3. The protons can be translocated to the matrix through the reaction ($EH_3 \rightarrow H_3E$) or $EH_3 \rightarrow H_3E^*$. A transition to state H_3ES can follow binding one ADP molecule from the matrix (represented as D_m) under constant phosphate (P_i) concentration, which is kept at 20 mM. This is followed by the production of one molecule of ATP (T_m) through the reaction $H_3ES \rightarrow H_3E + T_m$. Finally, in the transition $H^3E \rightarrow {}^{-3}E + 3H^+_m$ three protons are unbound in the matrix. The negative charged cavity of the enzyme can also transition from facing the matrix (state ${}^{-3}E$) to facing the IMS (state E^{-3}).

Transition 6 → 5 accounts for the binding of 3 protons from the IMS to the free enzyme (state 6, E^{-3}), two transitions can occur from here: transition 5 → 4 represents the transport of the protons to the matrix or transition 5 → 2 that represents the transport of the protons to the matrix without producing ATP. In state 4, ADP can bind to the enzyme (transition 4 → 3) and subsequently ATP can be synthesized (transition 3 → 2). This is followed by the unbinding of the protons in the matrix (transition 2 → 1), arriving at state 1.

List of Reactions for the ATP synthase model: (1) $^{-3}E + 3H^+_m \leftrightarrow H_3E$, k_{12}, k_{21} (2) $H_3E + T_m \leftrightarrow H_3ES$, k_{23}, k_{32} (3) $H_3ES \leftrightarrow H_3E^* + D_m$, k_{34}, k_{43} (4) $H_3E^* \leftrightarrow EH_3$, k_{45} , k_{54} (5) $EH_3 \leftrightarrow E^{-3} + H^+_i$, k_{56}, k_{65} (6)$E^{-3} \leftrightarrow {}^{-3}E$, k_{61}, k_{16}

Parameter values for the ATP synthase model: $k_{43} = 2\times10^6\ M^{-1}\ s^{-1}$, $k_{34} = 100\ s^{-1}$, $k_{12} = 25\ s^{-1}$, $k_{21} = 40\ s^{-1}$, $k_{65} = 3969\ s^{-1}$, $k_{56} = 1000\ s^{-1}$, $k_{61} = 33989\ s^{-1}$, $k_{16} = 146516\ s^{-1}$, $k_{54} = 1\times10^2\ s^{-1}$, $k_{45} = 100\ s^{-1}$, $k_{25} = 5.85\times10^{-30}\ s^{-1}$,$k_{52} = 1\times10^{-20}\ s^{-1}$, $k_{32} = 5\times10^3\ s^{-1}$, $k_{23} = 5\times10^6\ M^{-1}\ s^{-1}$

Modeled distribution of ATP synthases: The density of ATP synthases has been estimated at 3070 ATP synthases per um^2 in areas of high membrane curvature[165], this is consistent with ATP synthase densities estimated from yeast [166]. For each reconstruction, we calculated the surface area formed by vertices with first principal curvature higher than 70 μm^{-1}, and with this the number of ATP synthases was estimated for each organelle. For instance, the surface area of high curvature for the reconstruction of an SFA2 mitochondria is 0.144 μm^2, which leads to an

estimation of 433 units of ATP synthases in this reconstruction. To perform the spatial simulations, ATP synthases were distributed randomly in the regions of high curvature. For each mitochondrion, the total number of ATP synthases was kept the same.

ATP/ADP translocator (ANT) model: The model for the ATP/ADP translocator (ANT) is composed of 11 states and 22 chemical reactions, listed below. The kinetic diagram is presented in Figure S3F. The free protein is represented with the letter L in the diagram; it can bind ADP (D) or ATP (T) molecules from the matrix side (on the right) or IMS side (on the left), forming a triple molecular state. State TLD for instance represents a state with one ATP bound from the IMS and one ADP from the matrix side. The reaction that transports ATP from the matrix to the IMS is DLT → TLD, the rate constant for this reaction is k_p, the reverse reaction imports ATP to the matrix and exports ADP to the IMS, with rate constant k_{cp}. Futile translocations can also occur translocating one molecule of ATP by another ATP (TLT → TLT'). TLT and TLT' represent the same state, but they are differentiated to measure the rate of these translocations.

List of Reactions for the ANT model: (1) $T_m + L \leftrightarrow LT$, k^+_{Tm} , k^-_{Tm} (2) $D_m + L \leftrightarrow LD$, k^+_{Dm} , k^-_{Dm} (3) $T_i + L \leftrightarrow TL$, , k^+_{Ti} , k^-_{Ti} (4) $D_i + L \leftrightarrow DL$, k^+_{Di} , k^-_{Di} (5) $T_i + LT \leftrightarrow TLT$, k^+_{Ti} , k^-_{Ti} (6) $D_i + LT \leftrightarrow DLT$, k^+_{Di} , k^-_{Di} (7) $T_i + LD \leftrightarrow TLD$, k^+_{Ti} , k^-_{Ti} (8) $D_i + LD \leftrightarrow DLD$, k^+_{Di} , k^-_{Di} (9)TLD → DLT, k_{cp} (10) DLT → TLD, k_p (11) TLT → TLT', k_t (12) TLT' → TLT, k_t (13) DLD → DLD', k_d (14) DLD → DLD, k_d

Parameter values for the ANT model at Δϕ 180 mV: $k^-_{Tm} = 4\times10^4\ s^{-1}$, $k^+_{Tm} = 6.4\times10^6\ M^{-1}\ s^{-1}$, $k^-_{Ti} = 200\ s^{-1}$, $k^+_{Ti} = 4\times10^5\ M^{-1}\ s^{-1}$,$k^-_{Dm} = 4\times10^4\ s^{-1}$, $k^+_{Dm} = 4\times10^6\ M^{-1}\ s^{-1}$, $k^-_{Di} = 100\ s^{-1}$, $k^+_{Di} = 4\times10^6\ M^{-1}\ s^{-1}$, $k_p = 92\ s^{-1}$, $k_{cp} = 3.5\ s^{-1}$, $k_d = 4.8\ s^{-1}$, $k_t = 5.8\ s^{-1}$

Modeled distribution of ANTs: The density of ANTs has been estimated at 0.2 nm/mg protein in rat liver mitochondria[167]. Assuming that 1 nm/mg protein is approximately 1.25 mM[160] leads to a concentration of 0.25 mM. With this concentration, the number of ANTs in a given reconstruction can be estimated. Using the total mitochondrial volume proportionality with ANT concentration, we set the number of ANTs in SFA2 as 7678. In the onion mitochondrion, the number of ANTs were set at 7531. Thus, both types of mitochondria analyzed contained a 17:1 ratio of ANTs to ATP synthases.

VDAC model: To model the exit of ATP molecules to the cytosol we included VDACs, the main mechanism for metabolites to cross the OM. We implemented a simple model assuming VDAC proteins interact with ATP molecules and translocate them to the cytosol by the reaction VDAC + $ATP_{IMS} \rightleftharpoons$ VDAC + ATP_{cyto}. In all simulations, VDAC proteins were homogeneously distributed in the OMM. VDAC abundances were set as proportional to the total mitochondrial volume encapsulated by the OMM.

Parameters for the VDAC mode: rate constant of the reaction, $k_{vdac} = 1\times10^6\ M^{-1}\ s^{-1}$, the density of VDACs[168], δ = $1\times10^4\ \mu m^{-2}$, the number of VDACs considered in the simulations, N_{vdac} = 10268 for CM-containing SFA2 mitochondria and 4979 for onion-like SFA4 mitochondria.

Metabolite buffers: ATP and ADP molecules can interact with different cations, be bound, or ionized. The total concentration of ATP and ADP molecules can be distributed in several compounds like ATP^{4-}, ADP^{3-}, $ATPMg^{2-}$, etc. The final distributions can be estimated by coefficients representing the fraction of unbound ATP in the matrix or the IMS. For our model, mitochondrial ADP^{3-} and ATP^{4-} concentrations were estimated analogously to published data [160] as $[ADP]_{m,free} = 0.8\ [ADP]_m$, $[ATP]_{m,free} = [ATP]_m$, $[ATP^{4-}] = 0.05\ [ATP]_{free}$ and $[ADP^{-3}] = 0.45\ [ADP]_{free}$. The initial concentrations of ATP and ADP in the matrix were set to 13 mM and 2 mM,

respectively, and to 6.5 mM and 0.1 mM in the IMS and cytosol. In some simulations, these concentrations were kept constant.

Well-mixed model of ATP generation: A system of ordinary differential equations was derived from the reactions above (given in[159]) and used to calculate the rate of ATP generation in a well-mixed model, without considerations of mitochondrial geometry.

Molecular dynamics simulations

Coarse grained molecular dynamics models of systems with varying compositions were generated using insane.py[169] and Martini 2.2 force-field parameters[170,171]. Minimization and equilibration followed the conventional protocols established by CHARMM-GUI[172,173], summarized briefly here. Initial soft-core minimization is followed by steepest descent to generate an integrator ready relaxed configuration. The systems are jumped to 303 K by random assignment of velocities and the systems undergo several steps of NPT restrained equilibration. All equilibration steps were run with the Berendsen barostat[174]. Over the course of restrained equilibration stages, the timestep was gradually increased from 2 to 20 fs, and bilayer headgroup restraints were reduced from 200 to 20 KJ/mol nm^2. Systems are followed by several microseconds of NPT production using a semiisotropic Parinello-Rahman barostat[175]. All equilibration and production simulations use the Bussi-Donadio-Parinello velocity-rescaling thermostat[176] with reaction-field electrostatics and shifted Van der Waals potentials both with 1.1 nm cutoff[177]. Molecular dynamics simulations were run using gromacs 2022.1[178,179]. Force-field parameters, topologies, and simulation control parameters to reproduce this work are available https://github.com/RangamaniLabUCSD/2022-mitochondria-lipidomics-md. Henceforth all timescales reported are in simulation time, and not scaled using the conventional factor of 4 for Martini 2.2 simulations.

The bending modulus of the membrane for each composition was estimated by analyzing the height fluctuation spectra[74,76,80,180,181] of systems approximately 40 by 40 nm in size over 5 μs of production. Assuming the Helfrich Hamiltonian in the limit of small deformations (Monge gauge), zero membrane tension, and equipartition of energy, the power spectrum of the bilayer height fluctuations is given by,

$$< |h(\mathbf{q})|^2 > \; = \frac{k_B T}{L^2 K_c q^4},$$

Where q is the magnitude of wave-vector $\mathbf{q}$, $k_B T$ is the Boltzmann constant and temperature, L is the system length, and K_c is the membrane bending modulus. Quadrilateral meshes representing the surfaces of each leaflet are fit to the headgroup region (defined by the pointcloud of PO4 and GL0 beads) using piecewise cubic interpolation. The neutral surface of the bilayer was assumed to be the mean of the two surfaces. Computing the squared discrete fourier transform of the neutral surface, we obtained the 2D power spectrum of height fluctuations. The 2D power spectrum was converted into 1D for subsequent analysis by radially binning and averaging. Fitting the 1D power spectrum to the theoretical enables the estimation of the membrane bending modulus. Quantifying the error of the estimate is performed using parametric bootstrapping analysis following recommendations by Erguder and Deserno[181]. In brief, we have a sequence of mean squared amplitudes, $< |h(\mathbf{q})|^2 >$ for each q corresponding to each trajectory frame. To obtain a meaningful error we consider these as samples from a continuous trajectory with some potential correlation. Statistical block averaging enables us to estimate the autocorrelation time of the data and further a correlation corrected standard deviation. The standard error of the bending modulus is determined from using parametric bootstrapping to sample values of spectral power for large wavenumbers. These are subject to

a non-linear fit to obtain a distribution of K_c values for each system from which we obtain the standard deviation. Processing of the data for the analysis was performed using numpy[182], Scipy[183], MDAnalysis[183], and a modified curvature analysis framework[184] available from https://github.com/ctlee/membrane-curvature.

The local neighbor enrichment for each lipid type was investigated using MDAnalysis[183]. For each lipid, we count the numbers and types of each lipid within a 1.5 nm radius. The position of each lipid was either the sole PO4 or GL0 bead in the headgroup region. Normalizing by the number of frames and copy number of each lipid type produces the mean number of lipids of each type around a lipid of a given type; Comparing this value against the probability derived from random chance with no interactions given by the system composition, we obtain the deviation from random chance.

Using smaller systems of approximately 15 by 15 nm in length we computed the lateral pressure profiles for each composition. Each small system was equilibrated for 4 μs followed by 200 ns of production with positions and velocities written out every 5 ps in full numerical precision. The stresses for each frame by reprocessing using gmx-ls in gromacs 2016.3[185]. Contours for stress calculation were spaced approximately 1 nm in the X and Y directions (in-plane of the membrane) and 0.1 nm in the Z direction (normal to the membrane). The lateral pressure, $p(z)$, is given by $p(z) = \sigma_{ZZ} - (\sigma_{XX} + \sigma_{YY})/2$, where σ_{XX}, σ_{YY}, and σ_{ZZ} are the diagonal components of the stress tensor. The discrete lateral pressure profile was fit using a piecewise cubic interpolation and the bending moment, $K_c c_0 = \int_0^\infty zp(z)dz$, was evaluated using numerical integration of the interpolated function. Errors of values derived from and the lateral pressure profile were estimated by splitting the collected production frames into three non-overlapping chunks.

Continuum modeling of tubular cristae formation

Overview of the model: The mathematical derivations of this model can be found in extensive detail in[103]. Here, we provide a brief summary of the equations. The membrane is modeled as a thin elastic shell in mechanical equilibrium. Table 1 summarizes the symbols and notation; all nonscalar quantities are denoted by a bar overhead.

Table 1: Notation and list of symbols

Notation	Description	Unit
W	Free energy density of the membrane	pN/nm
κ	Bending modulus of the membrane	pN · nm
κ_d	Deviatoric modulus of the membrane	pN · nm
$\bar{n}$	Surface normal	1
$a_{\alpha\beta}$, $a^{\alpha\beta}$	Metric tensor and its contravariant	–
$b_{\alpha\beta}$, $b^{\alpha\beta}$	Curvature tensor and its contravariant	–
$\bar{T}$	Surface traction	pN/nm
s	Arclength along the membrane	nm
ψ	Angle made by surface tangent with the horizontal direction	1
H	Mean curvature	nm^{-1}
D	Deviatoric curvature	nm^{-1}
C_0	Spontaneous mean curvature	nm^{-1}
D_0	Spontaneous deviatoric curvature	nm^{-1}

f^{α}	Tangential component of the force per unit area	pN/nm^2
f_n	Normal component of the force per unit area	pN/nm^2
λ	Membrane tension	pN/nm
λ_0	Tension at boundary	pN/nm
F_n	Traction at the boundary	pN/nm

The force balance on the membrane is given by

$$\overline{T}^{\alpha}_{;\alpha} + p\,\overline{n} + \overline{f} = 0 \qquad \text{(S1)}$$

where, $\overline{f} = f^{\alpha}\overline{a}_{\alpha} + f^{n}\overline{n}$ is the external force density applied to the membrane, p is normal pressure on the membrane and $\bar{T}$ is traction on the membrane and given by,

$$\overline{T}^{\alpha} = N^{\beta\alpha}\overline{a}_{\beta} + S^{\alpha}\overline{n} \qquad \text{(S2)}$$

Here, $\bar{N}$ in-plane components of the stress and is given by

$$N^{\beta\alpha} = \zeta^{\beta\alpha} + b^{\beta}_{\mu}M^{\mu\alpha} \text{ and } S^{\alpha} = -M^{\alpha\beta}_{;\beta} \qquad \text{(S3)}$$

where, $\zeta^{\beta\alpha}$ and $M^{\beta\alpha}$ are obtained from the following constitutive relationships [186]

$$\zeta^{\beta\alpha} = \rho\left(\frac{\partial F}{\partial a_{\alpha\beta}} + \frac{\partial F}{\partial a_{\beta\alpha}}\right) \text{ and } M^{\beta\alpha} = \rho\left(\frac{\partial F}{\partial b_{\alpha\beta}} + \frac{\partial F}{\partial b_{\beta\alpha}}\right), \qquad \text{(S4)}$$

with $F = W/\rho$ is the energy mass density of the membrane. Combining these we get the balance equations in tangent and normal direction

$$N^{\beta\alpha} - S^{\alpha}b^{\beta}_{\alpha} + f^{\alpha} = 0, \quad S^{\alpha}_{;\alpha} + N^{\beta\alpha}b_{\beta\alpha} + p + f_n = 0 \qquad \text{(S5)}$$

Here f^{α} and f_n are the tangential and normal components of external force applied to the membrane per unit area.

The energy density of the membrane W is taken as follows to account for the mean and the deviatoric curvature

$$W = \kappa(H - C_0)^2 + \kappa_d(D - D_0)^2. \qquad \text{(S6)}$$

To obtain tubular shapes, recasting the Helfrich energy in terms of the isotropic spontaneous curvature C_0 and the anisotropic spontaneous curvature D_0, is a commonly used approach[103,187–189]. In this case, the energy is written in terms of the mean curvature and the deviatoric curvature D. The deviatoric curvature is defined as half of the difference between the two principal curvatures.

The tangential force balance relation in Equation (S5)$_I$ simplifies as

$$\lambda' = 2\kappa(H - C0)C' + 2\kappa_d(D - D0)D_0' - f^s. \qquad \text{(S7)}$$

The normal force balance relation S5$_{II}$ (the shape equation) becomes

$$p = \frac{L'}{r} + W_H(2H^2 - K) - 2H(W + \lambda - W_D D) - f_n \quad , \qquad \text{(S8)}$$

where L relates to the expression of the traction, given by

$$\frac{L}{r} = \frac{1}{2}\left(W_H' - W_D'\right) - \frac{\cos\psi}{r} W_D = - F_n. \quad \text{(S9)}$$

where F_n is the traction acting normal to the membrane. The above relation gives a natural boundary condition for *L* at both the boundaries. At the center, it directly correlates with the value of pulling force as

$$p_f = \lim_{r \to 0} 2\pi r F_n = - 2\pi L(0). \quad \text{(S10)}$$

Area parameterization: The governing equations are solved in a patch of the membrane with fixed surface area, where the coat area of protein is prescribed. The arclength parametrization poses some difficulties since the total arclength varies depending on the equilibrium shape of the membrane. Therefore, we did a coordinate transformation of arclength to a local area *a* as given by

$$\frac{\partial}{\partial s} = 2\pi r \frac{\partial}{\partial a} \quad \text{(S11)}$$

Note that in the differential form, local area relates as $da = 2\pi r\, ds$

The tangential force balance relation in Equation S7 transforms to

$$\frac{\partial \lambda}{\partial a} = 2\kappa (H - C0) \frac{\partial C_0}{\partial a} + 2\kappa_d (D - D0) \frac{\partial D_0}{\partial a} - \frac{f^s}{2\pi r}. \quad \text{(S12)}$$

The normal force balance relation in Equation S8 becomes

$$p = 2\pi \frac{\partial L}{\partial a} + 2\kappa(H - C_0)(2H^2 - K) - 2H(W + \lambda - 2\kappa_d D(D - D_0)) - f_n \quad \text{(S13)}$$

where

$$\frac{L}{r} = \frac{\partial}{\partial a}\left(\kappa(H - C_0) - \kappa_d(D - D_0)\right) - \kappa_D (D - D_0)\frac{\cos\psi}{r}. \quad \text{(S14)}$$

Numerical methods: We solved the system of equations (Equation S11 to Equation S14) numerically to get the equilibrium shape of the membrane for a coat of protein at the center of an axisymmetric area patch. The solution domain is presented in Figure S5A, along with the input protein coat and the boundary conditions shown in Figure S5A. The protein coat includes both the spontaneous mean curvature cap and a combination of mean and deviatoric spontaneous curvature in the rest of the coat region (Figure S5B). Note that we introduced a shape variable ψ, which denotes the angle made by the tangent from its radial plane. The membrane is clamped at the domain boundary, where both the displacement and the angle $\psi = 0$. The membrane tension is also prescribed at the boundary. At the pole, ψ is taken to be zero, which indicates the smoothness at the center of the membrane. L is set to zero, indicating that there is no pulling force acting at the center.

To solve the system of equations, we used MATLAB-based bvp4c, a finite difference-based ODE solver with fourth-order accuracy (MATLAB codes are available https://github.com/Rangamani-lab/arijit_deviatoric_tube.2022). We used a nonuniform grid ranging from 1000 to 10000 points, with the finer grid towards the center. We used a large domain size of 10^6 nm^2 to avoid boundary effects but we show the results focusing on the membrane deformation (region enclosed by the dashed line in Figure S5C). The values of the different parameters used are given in the table

below.

List of parameters used in the simulations

Notation	Description	Range
C_0	Spontaneous mean curvature	0.01–0.035 nm^{-1}
D_0	Spontaneous deviatoric curvature	0–0.035 nm^{-1}
$\kappa = (\kappa_d)$	Bending modulus of the membrane	10-20 $k_B T$
a_{coat}	Coat area of protein	1.413×10^4 nm^2
a_{mem}	Total area of the membrane	5.65×10^5 nm^2
λ_0	Tension at boundary	0.01 pN/nm

Parameter ranges: The parameter ranges for the continuum model were chosen from the literature and from the CGMD simulations. The range of anisotropic spontaneous curvature induced by the ATP synthases was estimated from the CGMD simulations presented in[23] for a single ATP synthase dimer by estimating the two principal curvatures for the small deformation seen in Figure 1 of that work. Note that these estimates are obtained from digitizing the images and do not contain the information carried in the thermal fluctuations. The bending moduli range was in the range consistent with CG-MD calculations and previous experimental measurements. The tension and the coat area are free parameters in the model and were tuned such that we could obtain tubules of length and radius consistent with experimental measurements as shown in Figure 5B.

References

140. Symons, J.L., Cho, K.-J., Chang, J.T., Du, G., Waxham, M.N., Hancock, J.F., Levental, I., and Levental, K.R. (2021). Lipidomic atlas of mammalian cell membranes reveals hierarchical variation induced by culture conditions, subcellular membranes, and cell lineages. Soft Matter *17*, 288–297.

141. Kucerka, N., Tristram-Nagle, S., and Nagle, J.F. (2005). Structure of fully hydrated fluid phase lipid bilayers with monounsaturated chains. J. Membr. Biol. *208*, 193–202.

142. Jablin, M.S., Akabori, K., and Nagle, J.F. (2014). Experimental support for tilt-dependent theory of biomembrane mechanics. Phys. Rev. Lett. *113*, 248102.

143. Kaltenegger, M., Kremser, J., Frewein, M.P.K., Ziherl, P., Bonthuis, D.J., and Pabst, G. (2021). Intrinsic lipid curvatures of mammalian plasma membrane outer leaflet lipids and ceramides. Biochim. Biophys. Acta Biomembr. *1863*, 183709.

144. Frewein, M.P.K., Rumetshofer, M., and Pabst, G. (2019). Global small-angle scattering data analysis of inverted hexagonal phases. J. Appl. Crystallogr. *52*, 403–414.

145. Rak, M., and Tzagoloff, A. (2009). F1-dependent translation of mitochondrially encoded Atp6p and Atp8p subunits of yeast ATP synthase. Proc. Natl. Acad. Sci. U. S. A. *106*, 18509–18514.

146. Alper, H., Fischer, C., Nevoigt, E., and Stephanopoulos, G. (2005). Tuning genetic control through promoter engineering. Proceedings of the National Academy of Sciences *102*, 12678–12683. 10.1073/pnas.0504604102.

147. Degreif, D., de Rond, T., Bertl, A., Keasling, J.D., and Budin, I. (2017). Lipid engineering reveals regulatory roles for membrane fluidity in yeast flocculation and oxygen-limited growth. Metab. Eng. *41*, 46–56.

148. Ejsing, C.S., Sampaio, J.L., Surendranath, V., Duchoslav, E., Ekroos, K., Klemm, R.W., Simons, K., and Shevchenko, A. (2009). Global analysis of the yeast lipidome by quantitative shotgun mass spectrometry. Proceedings of the National Academy of Sciences *106*, 2136–2141. 10.1073/pnas.0811700106.

149. Klose, C., Surma, M.A., Gerl, M.J., Meyenhofer, F., Shevchenko, A., and Simons, K. (2012). Flexibility of a Eukaryotic Lipidome – Insights from Yeast Lipidomics. PLoS ONE *7*, e35063. 10.1371/journal.pone.0035063.

150. Surma, M.A., Herzog, R., Vasilj, A., Klose, C., Christinat, N., Morin-Rivron, D., Simons, K., Masoodi, M., and Sampaio, J.L. (2015). An automated shotgun lipidomics platform for high throughput, comprehensive, and quantitative analysis of blood plasma intact lipids. European Journal of Lipid Science and Technology *117*, 1540–1549. 10.1002/ejlt.201500145.

151. Herzog, R., Schwudke, D., Schuhmann, K., Sampaio, J.L., Bornstein, S.R., Schroeder, M., and Shevchenko, A. (2011). A novel informatics concept for high-throughput shotgun lipidomics based on the molecular fragmentation query language. Genome Biol. *12*, R8.

152. Herzog, R., Schuhmann, K., Schwudke, D., Sampaio, J.L., Bornstein, S.R., Schroeder, M., and Shevchenko, A. (2012). LipidXplorer: a software for consensual cross-platform lipidomics.

PLoS One *7*, e29851.

153. Gregg, C., Kyryakov, P., and Titorenko, V.I. (2009). Purification of Mitochondria from Yeast Cells. Journal of Visualized Experiments. 10.3791/1417.

154. Meisinger, C., Pfanner, N., and Truscott, K.N. Isolation of Yeast Mitochondria. Yeast Protocols, 033–040. 10.1385/1-59259-958-3:033.

155. Timón-Gómez, A., Pérez-Pérez, R., Nyvltova, E., Ugalde, C., Fontanesi, F., and Barrientos, A. (2020). Protocol for the Analysis of Yeast and Human Mitochondrial Respiratory Chain Complexes and Supercomplexes by Blue Native Electrophoresis. STAR Protoc *1*. 10.1016/j.xpro.2020.100089.

156. McDonald, K., and Müller-Reichert, T. (2002). Cryomethods for thin section electron microscopy. Methods Enzymol. *351*, 96–123.

157. Bauer, C., Herzog, V., and Bauer, M.F. (2001). Improved Technique for Electron Microscope Visualization of Yeast Membrane Structure. Microsc. Microanal. *7*, 530–534.

158. Edwards, J., Daniel, E., Kinney, J., Bartol, T., Sejnowski, T., Johnston, D., Harris, K., and Bajaj, C. (2014). VolRoverN: enhancing surface and volumetric reconstruction for realistic dynamical simulation of cellular and subcellular function. Neuroinformatics *12*, 277–289.

159. Garcia, G.C., Bartol, T.M., and Sejnowski, T.J. (2022). A Thermodynamically-Consistent Model for ATP Production in Mitochondria. bioRxiv, 2022.08.16.500715. 10.1101/2022.08.16.500715.

160. Magnus, G., and Keizer, J. (1997). Minimal model of beta-cell mitochondrial Ca2+ handling. Am. J. Physiol. *273*, C717–C733.

161. Bertram, R., Gram Pedersen, M., Luciani, D.S., and Sherman, A. (2006). A simplified model for mitochondrial ATP production. J. Theor. Biol. *243*, 575–586.

162. Saa, A., and Siqueira, K.M. (2013). Modeling the ATP production in mitochondria. Bull. Math. Biol. *75*, 1636–1651.

163. Kerr, R.A., Bartol, T.M., Kaminsky, B., Dittrich, M., Chang, J.-C.J., Baden, S.B., Sejnowski, T.J., and Stiles, J.R. (2008). Fast Monte Carlo Simulation Methods for Biological Reaction-Diffusion Systems in Solution and on Surfaces. SIAM J. Sci. Comput. *30*, 3126–3149.

164. Pietrobon, D., and Caplan, S.R. (1985). Flow-force relationships for a six-state proton pump model: intrinsic uncoupling, kinetic equivalence of input and output forces, and domain of approximate linearity. Biochemistry *24*, 5764–5776.

165. Acehan, D., Malhotra, A., Xu, Y., Ren, M., Stokes, D.L., and Schlame, M. (2011). Cardiolipin affects the supramolecular organization of ATP synthase in mitochondria. Biophys. J. *100*, 2184–2192.

166. Davies, K.M., Anselmi, C., Wittig, I., Faraldo-Gómez, J.D., and Kühlbrandt, W. (2012). Structure of the yeast F1Fo-ATP synthase dimer and its role in shaping the mitochondrial cristae. Proc. Natl. Acad. Sci. U. S. A. *109*, 13602–13607.

167. Forman, N.G., and Wilson, D.F. (1983). Dependence of mitochondrial oxidative phosphorylation on activity of the adenine nucleotide translocase. J. Biol. Chem. *258*, 8649–8655.

168. De Pinto, V., Ludwig, O., Krause, J., Benz, R., and Palmieri, F. (1987). Porin pores of mitochondrial outer membranes from high and low eukaryotic cells: biochemical and biophysical characterization. Biochim. Biophys. Acta *894*, 109–119.

169. Wassenaar, T.A., Ingólfsson, H.I., Böckmann, R.A., Tieleman, D.P., and Marrink, S.J. (2015). Computational Lipidomics with insane: A Versatile Tool for Generating Custom Membranes for Molecular Simulations. J. Chem. Theory Comput. *11*, 2144–2155.

170. Marrink, S.J., Risselada, H.J., Yefimov, S., Tieleman, D.P., and de Vries, A.H. (2007). The MARTINI force field: coarse grained model for biomolecular simulations. J. Phys. Chem. B *111*, 7812–7824.

171. Marrink, S.J., de Vries, A.H., and Mark, A.E. (2004). Coarse Grained Model for Semiquantitative Lipid Simulations. J. Phys. Chem. B *108*, 750–760.

172. Qi, Y., Ingólfsson, H.I., Cheng, X., Lee, J., Marrink, S.J., and Im, W. (2015). CHARMM-GUI Martini Maker for Coarse-Grained Simulations with the Martini Force Field. J. Chem. Theory Comput. *11*, 4486–4494.

173. Jo, S., Kim, T., and Im, W. (2007). Automated builder and database of protein/membrane complexes for molecular dynamics simulations. PLoS One *2*, e880.

174. Berendsen, H.J.C., Postma, J.P.M., van Gunsteren, W.F., DiNola, A., and Haak, J.R. (1984). Molecular dynamics with coupling to an external bath. J. Chem. Phys. *81*, 3684–3690.

175. Parrinello, M., and Rahman, A. (1981). Polymorphic transitions in single crystals: A new molecular dynamics method. J. Appl. Phys. *52*, 7182–7190.

176. Bussi, G., Donadio, D., and Parrinello, M. (2007). Canonical sampling through velocity rescaling. J. Chem. Phys. *126*, 014101.

177. de Jong, D.H., Baoukina, S., Ingólfsson, H.I., and Marrink, S.J. (2016). Martini straight: Boosting performance using a shorter cutoff and GPUs. Comput. Phys. Commun. *199*, 1–7.

178. Bauer, P., Hess, B., and Lindahl, E. (2022). GROMACS 2022.1 Source code 10.5281/zenodo.6451564.

179. Abraham, M.J., Murtola, T., Schulz, R., Páll, S., Smith, J.C., Hess, B., and Lindahl, E. (2015). GROMACS: High performance molecular simulations through multi-level parallelism from laptops to supercomputers. SoftwareX *1-2*, 19–25.

180. Brown, F.L.H. (2008). Elastic modeling of biomembranes and lipid bilayers. Annu. Rev. Phys. Chem. *59*, 685–712.

181. Ergüder, M.F., and Deserno, M. (2021). Identifying systematic errors in a power spectral analysis of simulated lipid membranes. J. Chem. Phys. *154*, 214103.

182. Harris, C.R., Millman, K.J., van der Walt, S.J., Gommers, R., Virtanen, P., Cournapeau, D.,

Wieser, E., Taylor, J., Berg, S., Smith, N.J., et al. (2020). Array programming with NumPy. Nature *585*, 357–362.

183. Virtanen, P., Gommers, R., Oliphant, T.E., Haberland, M., Reddy, T., Cournapeau, D., Burovski, E., Peterson, P., Weckesser, W., Bright, J., et al. (2020). SciPy 1.0: fundamental algorithms for scientific computing in Python. Nat. Methods *17*, 261–272.

184. E., B.-O. (2021). MDAnalysis Membrane Curvature Tool 10.5281/zenodo.5553452.

185. Vanegas, J.M., Torres-Sánchez, A., and Arroyo, M. (2014). Importance of Force Decomposition for Local Stress Calculations in Biomembrane Molecular Simulations. J. Chem. Theory Comput. *10*, 691–702.

186. Steigmann, D.J. (2018). Mechanics and Physics of Lipid Bilayers. In The Role of Mechanics in the Study of Lipid Bilayers, D. J. Steigmann, ed. (Springer International Publishing), pp. 1–61.

187. Kralj-Iglič, V., Pocsfalvi, G., Mesarec, L., Šuštar, V., Hägerstrand, H., and Iglič, A. (2020). Minimizing isotropic and deviatoric membrane energy - An unifying formation mechanism of different cellular membrane nanovesicle types. PLoS One *15*, e0244796.

188. Kabaso, D., Bobrovska, N., Gozdz, W., Gov, N., Kralj-Iglic, V., Veranic, P., and Iglic, A. (2012). On the role of membrane anisotropy and BAR proteins in the stability of tubular membrane structures. J. Biomech. *45*, 231–238.

189. Noguchi, H., Tozzi, C., and Arroyo, M. (2022). Binding of anisotropic curvature-inducing proteins onto membrane tubes. arXiv [cond-mat.soft].